# Adjoint Shape Optimisation of Rocket Engine Turbine Blades

in collaboration with Arianegroup


Bhupinder Singh Sanghera

Department of Aerospace Engineering

Delft University of Technology

A thesis submitted for the degree of

*Master of Science*

This thesis has been approved by the

supervisor: Dr. ir. M. Pini

Thesis promotion committee:

| | |
|---|---|
| *Internal members:* | |
| Dr. ir. M. Pini | Delft University of Technology |
| Prof. dr. ir. P. Colonna | Delft University of Technology |
| Dr. R.P. Dwight | Delft University of Technology |
| *External members:* | |
| Dr. ir. L. Souverein | Arianegroup |



*To be defended publicly on Monday the 30th of March, 2020 at 14:00.*

*This thesis is confidential and cannot be made public until March 30, 2020.*

An electronic version of this thesis is available at
http://repository.tudelft.nl/.

I declare that the present thesis is an original report of my research, has been written by me and has not been submitted in any other form for any other degree. All supporting published and unpublished literature and resources of others have been acknowledged in the text and a list of references is given in the bibliography.

*to my parents and siblings*

# Acknowledgements

I would like to express my gratitude and appreciation to my supervisor Dr. ir. Matteo Pini for his constructive criticism, insightful advice and encouragement throughout the process of researching and writing this thesis. I feel extremely grateful to have been under the guidance of someone who strives for excellence, considers intellectual property and open communication as fundamental, recognises mistakes and constantly promotes and puts into practice collaborations in view of strengthening the competences of his students and fellow colleagues. I would also like to thank my co-supervisor Dr. ir. Louis Souverein for his insightful expertise, advice and for inspiring my interest in the development of innovative technologies. And lastly, but by no means least, I wish to pay my special regards to the members of the Propulsion & Power group for their invaluable assistance and to my friends for their unparalleled support and profound belief in my abilities.

I dedicate this thesis to my parents and siblings, whose unconditional love and relentless support made it possible for me to reach this milestone.

# Abstract

Prior to the detailed design of turbines, turbomachinery engineers must rely on mean-line and throughflow models to come to a preliminary design. These models are based on empirical loss correlations and are often derived from cascade experiments and numerical analyses that are confined to the subsonic and transonic regime. Axial turbines for rocket propulsion applications are characterised by a near zero degree of reaction and supersonic stator vanes that yield a complex flow field, making the prediction of losses challenging with existing correlations. The goal of this study is to investigate the variation of loss generation in supersonic axial turbine stator vanes with the isentropic exit Mach number. The profile losses will be split into components that can be attributed to different loss generation mechanisms whose relative magnitude may point to where performance improvement can be made. The investigation is performed on stator vanes that are used in the first turbine stage of a 1MN-class gas generator cycle type rocket engine. The stator vanes will be optimised for the profile losses by exploiting a novel adjoint optimisation framework for turbomachinery and the effect on the exit flow field will be investigated. The computational risk will be mitigated to ensure that the feasibility of the research is not jeopardised. The successful outcome of this research will lead to supersonic loss characteristics of axial turbine stator vanes, reduced development costs, increased efficiency levels and pave the way for future work on optimisation methods for turbomachinery applications.

# Nomenclature

**Greek Symbols**

| | |
|---|---|
| $\alpha$ | absolute flow angle |
| $\boldsymbol{\alpha}$ | design variable vector |
| $\beta_w^*$ | disk friction coefficient |
| $\gamma$ | ratio of specific heats |
| $\delta$ | boundary layer thickness |
| $\delta_e$ | boundary layer kinetic energy thickness |
| $\delta_{ij}$ | Kronecker delta |
| $\epsilon$ | turbulence dissipation rate |
| $\eta$ | primary efficiency, turbine efficiency |
| $\eta_K$ | Kolmogorov length scale |
| $\theta$ | boundary layer momentum thickness |
| $\kappa$ | thermal heat conductivity |
| $\kappa_L$ | laminar thermal heat conductivity |
| $\kappa_T$ | eddy thermal heat conductivity |
| $\mu$ | dynamic viscosity |
| $\mu_L$ | laminar viscosity |
| $\mu_T$ | eddy viscosity |
| $\nu$ | kinematic viscosity |
| $\xi$ | energy loss coefficient |

| | |
|---|---|
| $\xi_{bl}$ | boundary layer energy loss coefficient |
| $\xi_{sw}$ | shock wave energy loss coefficient |
| $\xi_s$ | entropy generation coefficient |
| $\xi_{te}$ | trailing edge energy loss coefficient |
| $\xi_{tot}$ | total energy loss coefficient |
| $\rho$ | density |
| $\sigma_A$ | area-weighted standard mean deviation |
| $\tau_{ij}$ | viscous stress tensor |
| $\psi_N$ | stator loss coefficient |
| $\psi_R$ | rotor loss coefficient |
| $\omega$ | specific turbulence dissipation rate |

**Roman Symbols**

| | |
|---|---|
| $b$ | blade pitch |
| $c$ | axial chord |
| $C_d$ | dissipation coefficient |
| $c_p$ | specific heat at constant pressure |
| $c_v$ | specific heat at constant volume |
| $C_{pb}$ | base pressure coefficient |
| $D$ | outer diameter rotor |
| $D_s$ | specific diameter |
| $e$ | internal energy |
| $e_k$ | kinetic energy |
| $h$ | enthalpy, blade height |
| $J$ | cost function |

| | |
|---|---|
| $k$ | turbulent kinetic energy |
| $\mathbf{K}$ | stiffness matrix |
| $k, l$ | FFD degrees |
| $l$ | curvilinear abscissa |
| $l_0$ | integral length scale |
| $M$ | Mach number |
| $\dot{m}$ | mass flow rate |
| $N_s$ | specific rotational speed |
| $p$ | pressure |
| $\mathbf{P}_{m,n}$ | FFD control points |
| $p_b$ | base pressure |
| $Pr_L$ | laminar Prandtl number |
| $Pr_T$ | turbulent Prandtl number |
| $R$ | universal gas constant |
| $\mathbf{R}$ | residuals of flow governing equations |
| $Re$ | Reynolds number |
| $s$ | entropy |
| $S_{ij}$ | strain rate tensor |
| $T$ | temperature |
| $t$ | time, trailing edge thickness |
| $\hat{T}$ | dummy variable |
| $\mathbf{T}$ | projection matrix |
| $u$ | velocity |
| $\mathbf{u}$ | state variable vector |

| | |
|---|---|
| $\mathbf{v}$ | adjoint variable vector |
| $w$ | local passage width at the trailing edge, relative velocity |
| $\mathbf{X}$ | mesh points vector |
| $\mathbf{X}_s$ | surface mesh points vector |
| $x, y, z$ | Cartesian coordinates |
| $x_i$ | Cartesian coordinate in $i^{th}$ direction |
| $Y$ | stagnation pressure loss coefficient |
| $y_p$ | parametric coordinate in $p^{th}$ direction |

**Subscripts**

| | |
|---|---|
| 0 | stagnation conditions |
| 1 | initial state, upstream of shock, inlet stator |
| 2 | final state, downstream of shock, outlet stator |
| 3 | rotor outlet |
| $\delta$ | boundary layer edge |
| $bl$ | boundary layer |
| $i, j, k$ | coordinate indices |
| $inj$ | injected |
| $m, n$ | FFD control point indices |
| $max$ | maximum |
| $p, q$ | parametric coordinate indices |
| $ref$ | reference |
| $s$ | isentropic conditions |
| $x, y, z$ | Cartesian indices |

**Superscripts**

| | |
|---|---|
| $\dot{}$ | rate |
| $''$ | turbulent fluctuations |
| $\overline{\phantom{x}}$ | mean contribution of Reynolds averaging |
| $\sim$ | mean contribution of Favre averaging |
| $d$ | $d^{th}$ optimisation step |
| $M$ | mass-weighted average |

**Acronyms**

| | |
|---|---|
| $AD$ | Algorithmic Differentiation |
| $CAD$ | Computer Aided Design |
| $CFD$ | Computational Fluid Dynamics |
| $DNS$ | Direct Numerical Simulation |
| $FFD$ | Free Form Deformation |
| $FGMRES$ | Flexible Generalised Minimum Residual Method |
| $KKT$ | Karush-Kuhn-Tucker |
| $LES$ | Large Eddy Simulation |
| $LUSGS$ | Lower-Upper Symmetric Gauss-Seidel |
| $NS$ | Navier-Stokes |
| $NURBS$ | Non-Uniform Rational Basis Spline |
| $PDE$ | Partial Differential Equation |
| $RANS$ | Reynolds-Averaged Navier-Stokes |
| $SA$ | Spalart-Allmaras |
| $SLSQP$ | Sequential Least Squares Programming |
| $SST$ | Shear Stress Transport |

# Contents

# List of Figures

# List of Tables

# Chapter 1

# Introduction

This chapter serves as an introduction to the thesis and presents the research analysis and statement, research objective and thesis outline.

## 1.1. Research Analysis and Statement

The development of liquid rocket propulsion is closely tied to the history of turbines and nowadays they are indispensable for efficient operation of high thrust liquid rocket engines. Turbines are applied in rocket engines to drive turbopumps that force propellants into the high pressure combustion chamber; forcing the propellants by pressurising the tanks is often not feasible because the pressure required for acceptable combustion pressure results in heavy propellant tanks. As a result, turbines alongside with turbopumps have become the backbone of large liquid rocket propulsion systems.

Supersonic axial turbines find their application in rocket engines because they are characterised by a high pressure ratio and therefore have the potential for large specific work. For a given power level, this type of turbine requires a small amount of driving fluid and a small number of stages. Despite that they generally operate at lower efficiency levels, the supersonic turbine may still be the best design choice for applications where the primary design requirements are a minimum number of stages and a minimum fluid consumption. In this case, the availability of high specific work more than compensates for the lower turbine efficiency.

To ensure that turbine designs lie within acceptable limits for rocket propul-

sion applications, the turbomachinery engineer must perform a trade-off between several parameters, for instance power, efficiency, reliability and cost. Efficiency is presumably one of the most important design parameters for turbomachinery. Turbomachinery engineers cope with stringent mass requirements and therefore, given that other performance criteria are satisfied, improving the efficiency is often the only means to reduce the number of stages or the fluid consumption. To increase the efficiency of turbines, the physical origins and effects of losses on turbine performance have to be thoroughly understood rather than indiscriminately using the available loss prediction correlations.

Over the past decades, tremendous efforts have been put into improving the efficiency of turbines. Accomplishing further performance improvements has therefore become more difficult, however, not impossible. The ever-advancing knowledge of the complex fluid mechanics and thermodynamics has pushed modern turbines to the extreme edge of technological development. Theoretical and experimental methods applied to both individual components and whole machines have made this progression achievable. Particularly the advancements of numerical methods for Computational Fluid Dynamics (CFD) and optimisation techniques such as the adjoint method have greatly improved our ability to understand turbines and to push performance abilities to extreme limits.

The development of modern axial flow turbines starts with the preliminary design phase during which the profile, tip-leakage and endwall losses must be modelled. The initial design configuration is defined from mean-line and throughflow models that are based on empirical loss correlations. Over the past decades, many loss correlations have been developed and are available in literature, but these are often derived from cascade experiments and numerical analyses that are confined to the subsonic or transonic regime. Axial flow turbines for rocket applications are characterised by a near zero degree of reaction and supersonic stator vanes that yield a complex flow field, making the prediction of losses challenging with existing correlations. The research statement can therefore be phrased as:

*The design of supersonic axial turbines for rocket propulsion applications remains challenging because the influence of loss mechanisms on the overall efficiency is not fully understood.*

## 1.2. Research Objective

The present study aims to unravel the physical origins of the profile loss mechanisms and the influence of the isentropic exit Mach number on the overall two-dimensional efficiency of supersonic axial stator vanes for rocket propulsion applications. Although the importance of three-dimensional loss mechanisms is acknowledged, this kind of study is considered to be beyond the scope of this research. The tip-leakage and endwall loss mechanisms can be investigated in follow up research. The objective of this research is to offer a competitive advantage to Arianegroup through supersonic axial turbine stator vanes with reduced development costs, increased efficiency levels and loss characteristics to be used in the early design phase of supersonic stator vanes by extending the pioneering work by Mee et al. [1] to the supersonic regime. The research questions can therefore be phrased as:

- *What is the impact of the isentropic exit Mach number on the profile losses in supersonic axial turbine stator vanes for rocket propulsion applications?*
- *What reduction of the profile losses in supersonic axial turbine stator vanes for rocket propulsion applications can be achieved using the adjoint optimisation method?*

The successful outcome of this research will result in a step change in the performance of supersonic axial turbines for rocket propulsion applications, reduced development costs and will pave the way for future work on optimisation methods for turbomachinery applications.

## 1.3. Thesis Outline

In chapter 2 the characteristics of rocket engine turbines and two-dimensional loss mechanisms in axial flow turbines are reviewed. In chapter 3 the governing equations for compressible viscous flow are introduced. The challenges of turbulence modelling are considered and some numerical methodologies are briefly discussed; the Direct Numerical Simulation (DNS) approach, the Large Eddy Simulation (LES) approach and the Reynolds-Averaged Navier-Stokes (RANS) approach. The RANS methodology is described in more detail. In chapter 4 the governing equations for adjoint-based shape optimisation are presented, with special emphasis on the discrete approach. The adjoint-based optimisation framework is discussed in terms of the adjoint solver, surface parametrisation and mesh deformation, with reference to the computational tool adopted in the present study. In chapter 5 the research methodology is presented; the optimisation setup and loss breakdown method are extensively described. The computational tool used in the present study is also introduced. In chapter 6 the findings of the current research are presented. The baseline and optimised design are investigated and compared using the loss breakdown method developed in chapter 5. In addition, this chapter provides a mesh sensitivity study, validation of the adjoint method and an investigation of the excitation on the adjacent blade row. In chapter 7 the research findings are summarised and their scientific and technical implications are discussed. Some suggestions for further works are also given.

# Chapter 2

# Rocket Engine Turbines

The current study presents an investigation of the two-dimensional loss generation in the stator vane of a supersonic axial flow turbine used in a gas generator cycle type rocket engine. Therefore, a description of rocket engine turbines and two-dimensional loss mechanisms in axial turbines must be provided.
The treatment in this chapter is intentionally brief as its purpose is to introduce the reader to rocket engine turbines and two-dimensional loss mechanisms in axial turbines. A detailed discussion on these topics however is too exhaustive and is clearly beyond the scope of this study. The reader is strongly recommended to read the detailed description of liquid rocket engine turbines by Douglas [2] and of all the loss mechanisms in turbomachinery by Denton [3].

## 2.1. Characteristics

Turbines are applied in rocket engines to drive the pumps that pressurise propellants and must therefore provide adequate power at the desired rotational speed and torque. The energy that drives the turbines is obtained by expanding a gaseous working fluid through one or more stages that consist of stator vanes and rotor blades mounted on disks to the shaft. The shaft speed is often limited by design considerations of the pump, logically leading to the use of axial flow turbines with their potential for higher efficiency at lower machine speeds. Figure 2.1 shows the liquid oxygen turbopump of the Vulcain 2 engine used in the European Ariane 5 launcher.

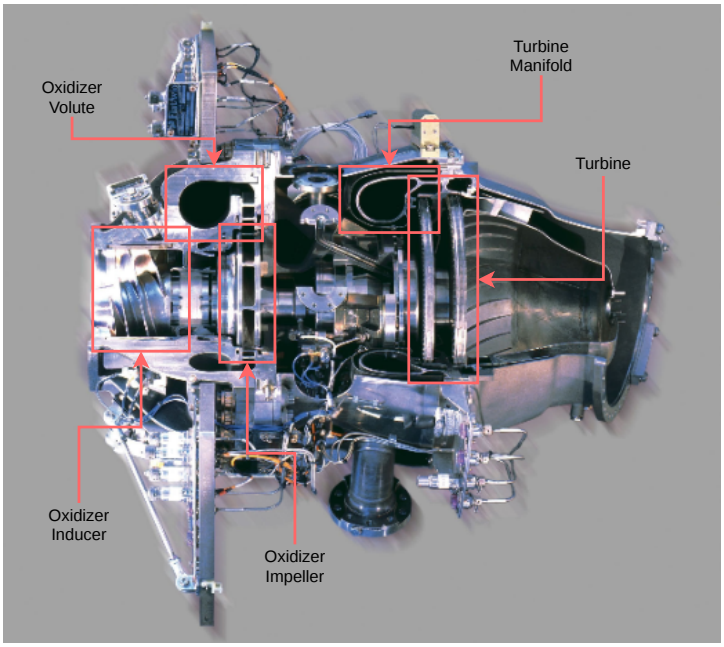


Figure 2.1: Liquid oxygen turbopump of the gas generator type Vulcain 2 engine used in the European Ariane 5 launcher (Paniagua and Steelant [4]).

### 2.1.1. Kinematics

The are two types of axial flow turbines that are most suited for use in rocket turbopumps: impulse turbines and reaction turbines. In an impulse turbine the conversion of enthalpy to kinetic energy takes place in the stator vanes and not in the rotor blades. The fluid expands to supersonic, nearly tangential, speeds through highly turning stator vanes and is then delivered to the rotor blades, where the kinetic energy is converted into a tangential force.

Momentum of the fluid that is imparted to the rotor blades causes the turbine wheel to rotate. In a velocity-staged impulse turbine all of the expansion takes place in the first-stage stator row. Stator vanes of the remaining stages merely turn the flow after it leaves the first-stage and direct the flow to enter the subsequent rotor rows in which energy from the working fluid is further imparted to the turbine wheel. The pressure-staged impulse turbine

splits the fluid expansion over all the stator rows. In a reaction turbine, the expansion of the working fluid is roughly equally divided between the stator and rotor rows. The pressure drop that is available in the working fluid of a gas generator cycle is typically very high and favors a simple, lightweight one- or two stage impulse turbine. Rocket turbines are typically low reaction turbines with a small expansion in the rotor blades. For example, the supersonic turbine stage investigated by Dorney et al. [5], typical of those proposed for a reusable launch vehicle, has a reaction of 0.092.

Supersonic axial flow turbines find their application in rocket engines because they are characterised by a high pressure ratio and therefore have the potential for large specific work. For a given power level, this type of turbine is driven by a small amount of working fluid and enables a reduction in the total number of stages. Supersonic turbines generally operate at lower efficiency levels which is an inevitable consequence of the high stage loading. However, when the primary design criteria are a minimum number of stages and a minimum fluid consumption, the supersonic turbine may still be the best design choice. In this case, the availability of high specific work and a low fluid consumption more than compensate for the lower turbine efficiency.

### 2.1.2. Design of Supersonic Nozzles

The design of supersonic stator vanes is based on the method of characteristics, which is a general technique for solving hyperbolic partial differential equations (PDE). The governing equations for the two-dimensional supersonic flow of a calorically perfect gas are of this type. The method of characteristics can be efficiently applied to design channels that produce uniform and parallel flows at supersonic speeds, which is desired for the flow entering the rotor rows.

The channels of a supersonic first-stage stator row consist of three sections; a converging section, a diverging section and a straight section on the suction surface. This is illustrated in Figure 2.2. The flow enters the stator row through the converging section in the axial direction and is ac-

celerated to sonic speed. This section is also designed to produce all of the required flow turning in order to keep the losses to a minimum. In the diverging section downstream of the throat the flow expands to the desired exit Mach number, producing expansion waves that are reflected off the centerline. The reflections of the expansion waves are cancelled to achieve uniform and parallel flow at the section exit. By making the throat edge sharper, nozzles with a smaller axial chord can be achieved that can serve as the basis for compactness considerations. The straight section on the supersonic suction surface completes the stator vane profile, and its length is determined by the required nozzle angle.

By designing the sections described above using the method of characteristics, an inviscid nozzle profile can be obtained, as indicated by the dashed lines in Figure 2.2. The viscid nozzle profile can be obtained by adding an estimate of the boundary layer displacement thickness to the diverging (supersonic) section of the profile, as indicated with the solid lines in Figure 2.2. The development of the boundary layer in the converging (subsonic) section is negligible.

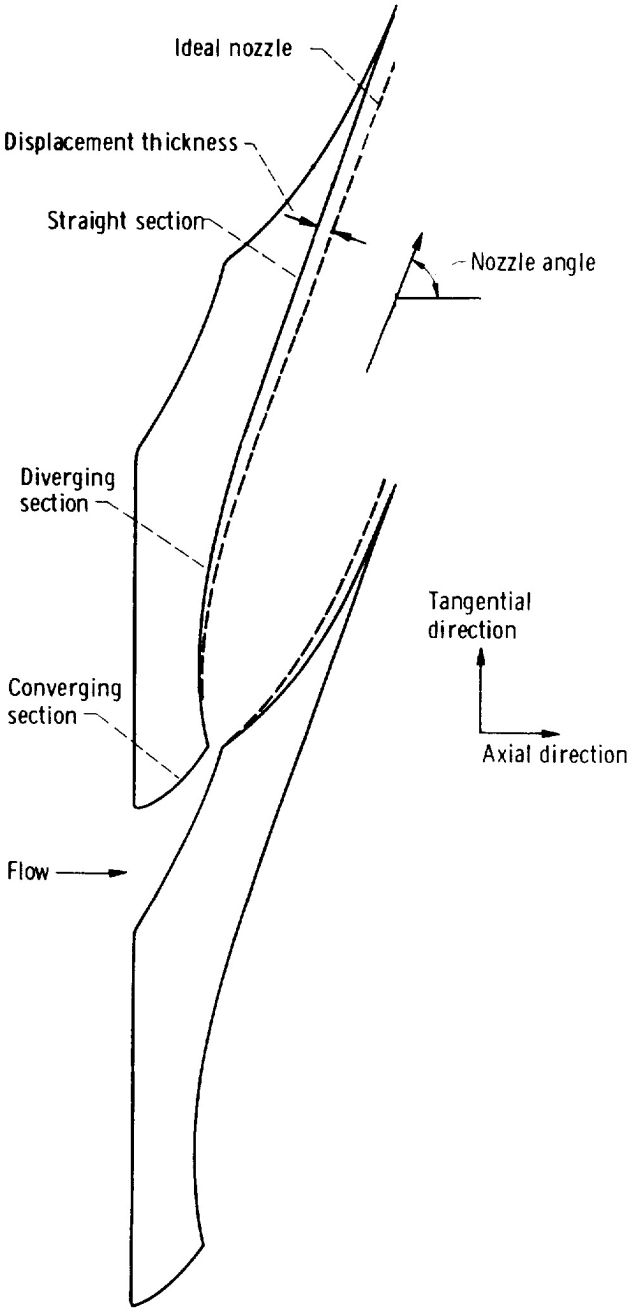


Figure 2.2: Design of a supersonic stator vane with a sharp-edged throat (Glassman [6]). A sharp-edged throat serves as the basis for the design of supersonic stator vanes with minimum axial length.

## 2.2. Two-Dimensional Loss Mechanisms

One of the most important performance parameters for turbines is undoubtedly the efficiency. A critical aspect in the analysis of these machines is the characterisation and assessment of losses that determine the efficiency. The most useful indicator of inefficiency in turbines is irreversible entropy generation; it can be regarded as lost work and therefore serves as a rigorous measure of loss. For a calorically perfect gas the specific entropy generation between two states is given by:

$$s_2 - s_1 = c_p \ln\left(\frac{T_{02}}{T_{01}}\right) - R\ln\left(\frac{p_{02}}{p_{01}}\right) \tag{2.1}$$

where $s$ is the entropy, T is the temperature, p is the pressure, $c_p$ is the specific heat at constant pressure, $R$ is the universal gas constant, the subscript 0 represents stagnation conditions and the subscripts 1 and 2 indicate the initial and final state, respectively. In an adiabatic flow the stagnation temperature is constant and so entropy generation is only determined by changes in stagnation pressure via:

$$s_2 - s_1 = -R\ln\left(\frac{p_{02}}{p_{01}}\right) \tag{2.2}$$

Hence for adiabatic flow, loss of stagnation pressure is formally identical to entropy generation.

The important sources of irreversible entropy creation are categorised by Greitzer [7] in a more practical manner in terms of fundamental internal flow processes as: viscous dissipation by friction in boundary layers, heat exchanges over finite temperature differences and mixing of mass, momentum and energy.

There are numerous loss mechanisms in axial flow turbines that lead to entropy generation and they can be categorised as two-dimensional or three-dimensional. The two-dimensional losses are those that would be present in a cascade test of a turbine blade row with infinite span and are often

referred to as the profile losses. The three-dimensional losses are the additional losses that exist in a turbine that operates in a realistic rotating arrangement.

The two-dimensional losses in a turbine blade row consist of the blade boundary layer loss, trailing edge loss and the shock loss. The three-dimensional loss sources can be separated into the tip-leakage loss, endwall loss and the loss due to coolant flows.

In the present study only two-dimensional losses will be investigated. Although the importance of the three-dimensional loss mechanisms is acknowledged, this kind of study is considered to be beyond the scope of this research. The tip-leakage and endwall loss mechanisms can be investigated in follow up research.

This historical breakdown of loss is illustrated in Figure 2.3 and continues to be widely used although it must be clearly recognised that the loss mechanisms are seldom really independent.

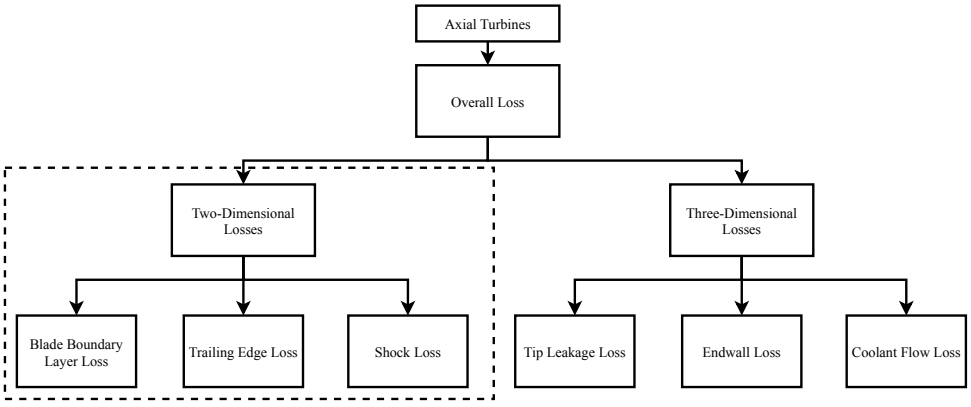


Figure 2.3: Traditional breakdown of the loss mechanisms in axial flow turbines. In the present study only the two-dimensional loss mechanisms are investigated.

### 2.2.1. Boundary Layer Loss

The boundary layer loss may be thought of as the lost work that is expended against the intense viscous shear within the boundary layers. A derivation by Denton [3] shows that the rate of change of entropy flux in a

two-dimensional boundary layer with the conditions of an adiabatic surface and boundary layer edge is given by:

$$\frac{d}{dx}\int_0^{\delta}\rho u_x\,(s-s_\delta)\,dy=\int_0^{\delta}\frac{1}{T}\tau_{xy}\left(\frac{du_x}{dy}\right)dy \tag{2.3}$$

where $x$ and $y$ are the Cartesian coordinates along and perpendicular to the blade surface, respectively, $\rho$ is the density, $u_x$ is the velocity in the x-direction, $\tau_{xy}$ is the shear stress with the Cartesian tensor notation, $\delta$ is the boundary layer thickness and the subscript $\delta$ refers to a quantity at the boundary layer edge. Equation 2.3 shows that the total rate of entropy production within boundary layers is proportional to the integral of shear stress over the boundary layer velocity profile. It is noteworthy to point out that for most boundary layers, especially for turbulent layers, the velocity gradients near the surface are the largest and thus the entropy creation is concentrated in the inner part of the layers. This corollary is also supported by Dawes [8], who presents a more comprehensive breakdown of entropy generation and shows that the inner boundary layers contribute to as much as 90% of the total entropy generation.

By examining Equation 2.3, Young [9], White [10] and Schlichting [11] found that for compressible flows:

$$\frac{d}{dx}\left(\rho_\delta u_\delta^3\delta_e\right)=T_\delta\int_0^{\delta}\frac{1}{T}\tau_{xy}\left(\frac{du_x}{dy}\right)dy \tag{2.4}$$

where $\delta_e$ is the boundary layer kinetic energy thickness. The cumulative rate of dissipation at a certain location along the blade is thus proportional to the kinetic energy thickness at that location. The rate of dissipation also scales as the cube of the free-stream velocity so that regions of high free-stream velocity such as the suction surface become dominant sources of loss generation.

The entropy production rate is frequently transformed into a dimensionless boundary layer dissipation coefficient for practical convenience:

$$C_d = \frac{T_\delta}{\rho_\delta u_\delta^3} \int_0^\delta \frac{1}{T} \tau_{xy} \left( \frac{du_x}{dy} \right) dy \tag{2.5}$$

where $C_d$ is the dissipation coefficient. Truckenbrodt [12] and Schlichting [11] have fit experimental data of the $C_d$ of laminar and turbulent boundary layers, respectively, to the momentum thickness Reynolds number $Re_\theta$. The results suggest that in the range of $Re_\theta$ where either a laminar or turbulent boundary layer could exist, the $C_d$ in the laminar boundary layer is much less than in the turbulent one; by a factor of between 2 and 5. This emphasises the essence of accurately anticipating the boundary layer transition in order to minimise the boundary layer losses.

### 2.2.2. Shock Loss

It is well known that shock waves are irreversible and that changes in the flow properties across it are nearly discontinuous. The discontinuities occur in extraordinarily short distances that are comparable with a few molecular mean free paths (Denton [3]) and give rise to large gradients of velocity and temperature. This leads to strong thermal conduction and large viscous normal stresses in the interior of the shock wave, making shock waves a source of entropy generation.

The equation for the entropy increase across a plane normal shock has been derived by many text books, e.g. by Shapiro [13]. This equation can be expanded in a power series for a weak shock:

$$\frac{s_2 - s_1}{c_v} \approx \frac{2\gamma(\gamma - 1)}{3(\gamma + 1)^3} \left(M_1^2 - 1\right)^3 + \mathcal{O}\left(M_1^2 - 1\right)^4 \tag{2.6}$$

where $c_v$ is the specific heat at constant volume, $M_1$ is the upstream Mach number, $\gamma$ is the ratio of specific heats and stations 1 and 2 refer to upstream and downstream of the shock, respectively. Equation 2.6 shows that the entropy generation due to a normal shock wave varies linearly with cube of $M_1^2 - 1$. Changes in the flow properties are relatively small for

upstream Mach numbers $M_1$ less than 1.4 (Anderson [14]). However, if the upstream Mach number further increases, these changes drastically increase and correspondingly the shock loss becomes significant (Dixon and Hall [15]).

Equation 2.6 is strictly applicable to normal shock waves. To apply Equation 2.6 to oblique shock waves, the upstream Mach number $M_1$ must represent the component normal to the oblique shock wave. Inclined shocks will therefore always produce less entropy compared to a normal shock with the same upstream Mach number.

There are various other loss mechanisms that can be indirectly attributed to the occurrence of shock waves in turbines; trailing edge shock system and shock wave-boundary layer interaction. The trailing edge shock system is a direct consequence of the low base pressure acting on the trailing edge; it causes an expansion of the flow around the trailing edge to this low base pressure. When the suction and pressure surface flows meet, they are recompressed by a strong shock. The loss generation arises from the strong viscous dissipation in the flow separation zone immediately downstream of the trailing edge and from the recompression shock.

The shock wave-boundary layer interaction can be attributed to the adverse pressure gradient that the boundary layer experiences when it passes a shock wave. If the shock is weak, usually a separation bubble forms at the root of the shock with subsequently extra dissipation within and downstream of the bubble. If the incoming boundary layer is laminar, the separation bubble will almost certainly cause transition of the boundary layer to a turbulent one. This will increase the $C_d$ significantly, as discussed in subsection 2.2.1, and consequently increase the boundary layer losses. If the shock is strong it may cause complete separation of the boundary layer, and Denton [3] states that this gives increased contribution to the base pressure term in Equation 2.8, leading to larger trailing edge losses. According to Atkin and Squire [16], a normal shock is likely to separate a boundary layer completely if $M_1$ is larger than 1.4. A more accurate approach is considered by Souverein et al. [17], who proposed a scaling to determine the

flow regime (attached, incipiently separation, fully separated), which also constitutes a separation criterion for shock induced separation. The separation criterion is only dependent on the free-stream Mach number and the deflection angle, and successfully classified the separation states for a wide range of shock wave-boundary layer interactions documented in literature over a large Reynolds and Mach number range.

### 2.2.3. Trailing Edge Loss

A frequently occurring situation in internal flow applications is the mixing of two streams of fluid at an angle with different stagnation conditions. The different streams are subjected to a shear strain rate upon mixing and generate entropy as a result of the viscous shear. Young and Wilcock [18] performed a differential analysis on this mixing situation which is not restricted to mixing at either constant area or pressure, and showed that the irreversible entropy creation per unit mass within the control volume can be given as:

$$\frac{ds}{c_p} = \frac{\dot{m}_{inj}}{\dot{m}} \left\{ \left[ \frac{\left(u_x^2 - u_{x,inj}^2\right) + u_{y,inj}^2}{2c_p T} \right] + \left[ \int_T^{T_{inj}} \left( \frac{1}{T} - \frac{1}{\hat{T}} \right) d\hat{T} \right] \right\} \tag{2.7}$$

where $\dot{m}$ is the mass flow rate, $\hat{T}$ is a dummy variable and the subscript 'inj' indicates the injected stream. The first term represents the dissipation of bulk kinetic energy as the two streams mix and their velocities equilibrate. The second term represents the thermal dissipation as the two streams mix and their temperatures equilibrate. Multiplying the latter term with $\dot{m}c_pT$ results in the power that could be obtained theoretically by a Carnot cycle coupled between the mainstream flow at temperature T and the injected stream at $T_{inj}$ (Young and Wilcock [18]). It is also noteworthy that all the kinetic energy injected perpendicular to the mainstream is dissipated.

The loss generated by the constant area mixing of a wake downstream of a blunt trailing edge for incompressible flow is examined by Denton [3] who

showed that the stagnation pressure loss coefficient $Y$ can be expressed as:

$$Y = -\frac{C_{pb}t}{w} + \frac{2\theta}{w} + \left(\frac{\delta + t}{w}\right)^2 \tag{2.8}$$

where $C_{pb}$ is the base pressure coefficient, $t$ is the trailing edge thickness, $w$ is the local passage width at the trailing edge and $\theta$ is the momentum thickness. The base pressure coefficient is defined as:

$$C_{pb} = \frac{p_b - p_{ref}}{0.5\rho u_{ref}^2} \tag{2.9}$$

where $p_b$ is the base pressure and the subscript ref indicates a reference value. The restriction of incompressible flow can be easily relaxed in numerical solutions. The first, second and last term in Equation 2.8 arise due to the loss generated by the low base pressure acting on the trailing edge, mixing of the momentum contained in the boundary layers and the simultaneous blockage of the boundary layers and the trailing edge, respectively.

### 2.2.4. Loss Trends

The variation of the loss components with the exit Mach number is shown in Figure 2.4 for a transonic turbine cascade at a Reynolds number $Re$ of $1 \times 10^6$. Measurements of the boundary layer towards the trailing edge of the suction surface and examination of the wake traverse data have allowed the individual loss contributions due to the blade boundary layers, shocks and trailing edge to be determined as energy loss coefficients.

The boundary layer loss decreases monotonically with the exit Mach number $M_2$ and significantly contributes to the overall loss for subsonic and transonic $M_2$. The results indicate that this trend continues for supersonic $M_2$.

The shock loss is intuitively negligible for $M_2 < 0.95$. For higher values of $M_2$ the shock loss considerably increases and the results suggest it settles and possibly drops for supersonic $M_2$. The contribution of the shock loss

to the overall loss is negligible for subsonic $M_2$ but relatively significant for transonic $M_2$.

The trailing edge loss increases with $M_2$, except for near sonic $M_2$. The contribution of the trailing edge loss to the overall loss is significant for subsonic $M_2$ and even more so for transonic $M_2$. The results suggest that this contribution further increases for supersonic $M_2$.

The total loss remains relatively constant for subsonic $M_2$ and this is related to the absence of shocks and large regions of boundary layer separation. The total loss suddenly increases for $M_2$ > 0.95 and this is associated to the appearance of shocks and the increased trailing edge loss contribution. The results suggest that the total loss levels off for supersonic $M_2$.

There are no similar studies in literature for supersonic turbines blades; the present study will investigate the loss trends in the supersonic regime.

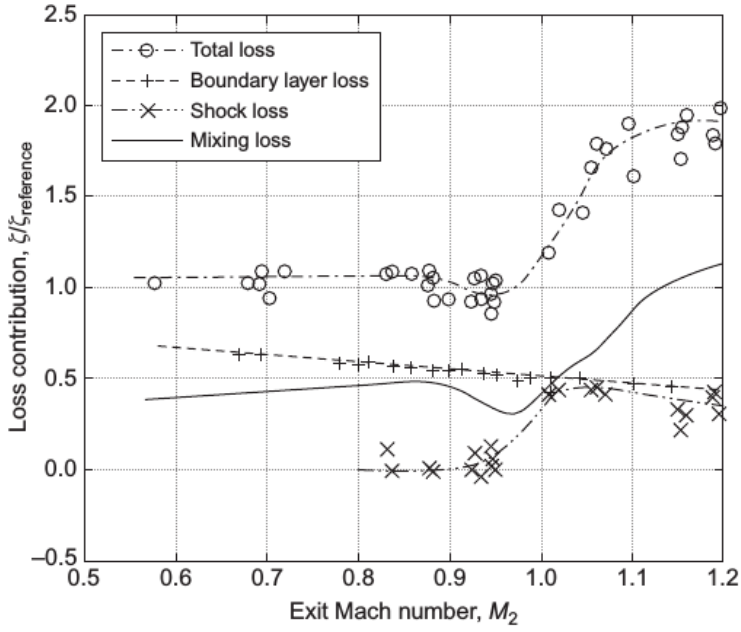


Figure 2.4: Experimental measurements of the variation of the energy loss coefficient $\xi$ with the exit Mach number $M_2$ for a transonic turbine cascade at a Reynolds number of $1 \times 10^6$ (Mee et al. [1]).

# Chapter 3

# Compressible Viscous Flow

The aim of the present study is to map the two-dimensional loss characteristics with the isentropic exit Mach number for axial flow turbines for rocket propulsion applications. Therefore, a theoretical background must be provided on compressible viscous flow theory.
The treatment in this chapter is deliberately concise as its purpose is to present the governing equations to give the reader an impression of compressible viscous flows. A comprehensive presentation of compressible viscous flows would be too exhaustive and is clearly beyond the scope of this study. For a more detailed description the reader is encouraged to closely examine the work of Anderson [14] and White [10].
In this chapter the Cartesian tensor form with the Einstein convention will be adopted.

## 3.1. Governing Equations

Compressible viscous flow is mathematically described by the governing equations derived from the principles of mass, momentum and energy conservation together with the continuum hypothesis. The governing equations are commonly called the Navier-Stokes (NS) equations and are probably the most pivotal equations in all of theoretical fluid mechanics. Although strictly speaking the term NS merely refers to the components of the momentum equation, it is common practise to include the mass and energy equation in the set referred to as the NS equations. In the present work this practise will be followed.

The conservation of mass is described by the continuity equation which relates the local variation of density in time to convective mass transport. The mass conservation equation for compressible viscous flow without source terms is given by:

$$\frac{\partial \rho}{\partial t} + \frac{\partial}{\partial x_i}(\rho u_i) = 0 \tag{3.1}$$

where t is the time and $u_i$ and $x_i$ are the velocity and the Cartesian coordinate in the $i^{th}$ direction, respectively.

The conservation of momentum equation relates the local change of momentum in time to convective momentum transport, surface forces due to pressure and fluid deformation, and to body forces. The influence of body forces is usually very small, especially in turbomachinery, and can therefore be neglected. The momentum conservation equation for compressible viscous flow without body forces and source terms is given by:

$$\frac{\partial}{\partial t}(\rho u_i) + \frac{\partial}{\partial x_j}\left(\rho u_j u_i\right) = -\frac{\partial p}{\partial x_i} + \frac{\partial \tau_{ij}}{\partial x_j} \tag{3.2}$$

where $\tau_{ij}$ is the viscous stress tensor. The viscous stress tensor models stresses that can be attributed to the time rate of strain.

The energy conservation equation can be inferred from the first law of thermodynamics and relates the local change of stagnation energy in time to conductive heat transport and to work done by pressure and viscous forces. The energy equation can take on many forms but in this study the energy equation is presented using the stagnation internal energy. The conservation of stagnation internal energy when omitting the work done by body forces and source terms is given by:

$$\frac{\partial}{\partial t}(\rho e_0) + \frac{\partial}{\partial x_j}\left(\rho h_0 u_j\right) = \frac{\partial}{\partial x_j}\left(u_i \tau_{ij}\right) + \frac{\partial}{\partial x_j}\left(\kappa \frac{\partial T}{\partial x_j}\right) \tag{3.3}$$

where $e$ is the internal energy, $h$ is the enthalpy and $\kappa$ is the thermal conductivity.

## 3.2. Turbulence

The governing equations of compressible viscous flow are called the NS equations and these are presented in section 3.1. The governing equations are a system of coupled and non-linear PDEs that hold for all flows without source terms, including laminar and turbulent flows. The exact analytical solution of the NS equations only exists in few situations where many terms in the governing equations are precisely zero due the physical and geometrical nature of the problem. This results in a set of equations for which the solution is easily attained analytically or by simple numerical methods. An assumption that is typically made for many of these cases is that the flow is laminar. However, most flows encountered in turbomachines are turbulent and therefore require special treatment.

The fluid motion in a turbulent flow is dictated by complex irregularities that originate from the interaction of viscous terms and non-linear terms, making a deterministic approach to turbulence problems difficult. Any perturbation applied to a turbulent flow results in an increasing number of random fluctuations which rapidly propagate in time and space. Applications such as rocket engine turbines are influenced by turbulent motions and therefore require a reliable numerical method that is able to overcome the problems arising in the mathematical solution of the NS equations.

### 3.2.1. Scales of Turbulent Motion

Turbulence is described by the energy cascade theory as an hierarchy of eddies of different scales. The turbulent kinetic energy is generated by the integral scale eddies which are unstable and break down in to inertial and dissipative scale eddies. The kinetic energy is redistributed from the integral scale to the dissipative scale in a process called turbulence energy cascade. While turbulence progresses towards the dissipative scale, the effects of viscosity become progressively more dominant and the turbulent kinetic energy is transformed into thermal energy. The redistribution of the kinetic energy from the integral range to the dissipative range is managed

by the inertial scale eddies for which the effects of viscosity are not so important. The rate at which kinetic energy is dissipated by the dissipative scale eddies can be assumed to be equal to the rate at which kinetic energy is supplied from the integral scales. This condition is called turbulence equilibrium and in this case the dissipative length scale (and time and velocity scales) can be completely described by dimensional arguments using the turbulence dissipation rate and the kinematic viscosity.

$$\eta_K = \left(\frac{\nu^3}{\epsilon}\right)^{\frac{1}{4}} \tag{3.4}$$

where $\eta_K$ is the Kolmogorov length, $\nu$ is the kinematic viscosity and $\epsilon$ is the turbulence dissipation rate. Tennekes and Lumley [19] have shown that the amount of kinetic energy per unit mass in the integral scale eddies is proportional to $u^2$ and that the rate of energy transfer to the smaller scales is proportional to $u/l_0$ where $l_0$ is the integral length scale. The rate of kinetic energy supply to the dissipative scales is thus of order $u^3/l_0$. The kinetic energy is dissipated at a rate $\epsilon$ and in the condition of turbulence equilibrium this should be equal to the energy supply rate:

$$l_0 \sim \frac{u^3}{\epsilon} \tag{3.5}$$

The ratio between the integral scale and the Kolmogorov scale can now be determined and gives an estimate of the number of turbulent structures contained in a single turbulent motion in one dimension:

$$\frac{l_0}{\eta_k} = Re^{\frac{3}{4}} \tag{3.6}$$

where $Re$ is the Reynolds number. It becomes evident from Equation 3.6 that for flows with a high Reynolds number, the turbulence structures vary on a vast range of length scales. This makes the challenge of directly solving the NS equations for flows with a high $Re$ computationally very expensive.

### 3.2.2. Modelling

The previous section sheds light on the difficulty of solving directly the NS equations for all turbulent structures in a flow. The necessity of resorting to numerical methodologies is without doubt unquestionable.

The most rigorous treatment of turbulence involves the direct solution of the NS equations without any further assumption and is labelled Direct Numerical Simulation (DNS). A DNS is computationally very expensive because it accurately resolves the length scales and time scales of all turbulent structures. Ferziger and Perić [20] have shown that for homogeneous isotropic turbulence, the simplest type of turbulence, the cost of a DNS scales with $Re^3$. The application of DNS is therefore not feasible for the high Reynolds number flows that are typically found in turbomachinery for rocket propulsion applications.

An alternate approach must therefore be considered; one which only accurately resolves the most important part of the wide range of length and time scales of a turbulent flow, and models the other part. In this approach, called Large Eddy Simulation (LES), the dynamics of the integral structures, which generally contain much more energy than the dissipative structures, are computed directly and the effects of the dissipative structures are modelled. The size and strength of the integral scale eddies make them without doubt the most dominant transporters of conserved flow quantities. Although LES is much less costly than DNS, it remains too costly for optimisation purposes and is therefore not suited for systematic investigations aimed at defining best practises for turbomachinery design.

A statistical approach is therefore considered; one where the flow variables are decomposed into a mean part and a fluctuating part. This approach is called Reynolds-averaged Navier-Stokes (RANS). The RANS equations can be obtained by averaging the non-linear NS equations which give rise to terms that must be modelled. In this approach all unsteadiness is averaged out, i.e. the governing equations are solved for the mean values which are the most attractive from an engineering point of view. Engineers are usually only interested in knowing a few properties of a turbulent flow.

Using higher-fidelity approaches like LES or DNS to determine these properties is, to say the least, unreasonable. In this regards, RANS represents a good compromise between accuracy and computational load. The RANS approach will therefore be utilised in the analysis of the present study.

## 3.3. Reynolds-Averaged Navier-Stokes

Turbulent flows are inherently unsteady, i.e. their flow patterns constantly change with time. It is possible however, to define a steady state where the averaged flow field is invariant with time. In this case, every variable can be decomposed into a mean and a fluctuating component. This procedure is called Reynolds averaging and involves different forms; the time-averaging variant will be adopted throughout the present work. The standard Reynolds decomposition of any linear term in the governing equations results in an averaged mean quantity, however, quadratic non-linear terms introduce two quantities; a product of the averages and a covariance. The covariance term corresponds to correlations involving density fluctuations and requires modelling. In the presence of density fluctuations it is therefore advised to apply Favre averaging to certain quantities to prevent additional covariance terms that considerable complicate the averaging procedure.

The NS equations presented in section 3.1 can be rewritten with the averaging formalism presented above. To avoid additional unclosed correlations, the pressure and density are averaged using the Reynolds procedure whereas all other variables are averaged using the Favre method. The averaged continuity equation can then be expressed as:

$$\frac{\partial \overline{\rho}}{\partial t} + \frac{\partial}{\partial x_i}\left(\overline{\rho}\,\widetilde{u}_i\right) = 0 \tag{3.7}$$

where the overbar implies the mean contribution of Reynolds averaging and the tilde indicates the mean contribution of Favre averaging. The averaged momentum conservation equation is given by:

$$\frac{\partial}{\partial t}\left(\overline{\rho}\widetilde{u}_i\right)+\frac{\partial}{\partial x_j}\left(\overline{\rho}\widetilde{u}_j\widetilde{u}_i\right)=-\frac{\partial\overline{p}}{\partial x_i}+\frac{\partial}{\partial x_j}\left(\tilde{\tau}_{ij}-\overline{\rho}\widetilde{u_i''u_j''}\right) \tag{3.8}$$

where the turbulent fluctuations are denoted by a double prime. The averaged stagnation internal energy conservation equation is given by:

$$\begin{aligned}\frac{\partial}{\partial t}\left(\overline{\rho}\widetilde{e_0}\right)+\frac{\partial}{\partial x_j}\left(\overline{\rho}\widetilde{h_0}\widetilde{u}_j\right)=\frac{\partial}{\partial x_j}\left(\kappa\frac{\partial\widetilde{T}}{\partial x_j}-\overline{\rho}\widetilde{u_j''h''}+\widetilde{\tau_{ij}u_i''}-\overline{\rho}\widetilde{u_j''k}\right)\\+\frac{\partial}{\partial x_j}\left[\widetilde{u}_i\left(\tilde{\tau}_{ij}-\overline{\rho}\widetilde{u_i''u_j''}\right)\right]\end{aligned} \tag{3.9}$$

where $k=\frac{1}{2}u_iu_i$ is the turbulent kinetic energy. Strictly speaking, these equations are called the Favre-averaged RANS equations, but it is a common practise to refer to them as the RANS equations. This practise will be adopted throughout the present study.

The RANS equations can be taken to be synonymous with the NS equations with the exception of some additional terms that require modelling. Closure of Equation 3.7 to Equation 3.9 requires the transport of momentum due to turbulent fluctuations, denoted by Favre-averaged Reynolds-stress tensor $\overline{\rho}\widetilde{u_i''u_j''}$, and the turbulent heat transport $\frac{\partial}{\partial x_j}\left(\overline{\rho}\widetilde{u_j''h''}\right)$ to be supplied. The Favre-averaged turbulent kinetic energy is often omitted or obtained using a turbulence model.

The Bousinessq eddy viscosity hypothesis is an attractive approach to achieve the aforementioned closure. This approach assumes that the turbulent shear stress is linearly related to the mean rate of strain. The basic idea is that the integral scale eddies predominantly influence momentum transfer in turbulent flows. The Boussinesq eddy viscosity hypothesis for compressible RANS reads:

$$-\overline{\rho}\widetilde{u_i''u_j''}=2\mu_T\tilde{S}_{ij}-\frac{2}{3}\mu_T\tilde{S}_{kk}\delta_{ij}-\frac{2}{3}\overline{\rho}\widetilde{k}\delta_{ij} \tag{3.10}$$

$$\tilde{S}_{ij}=\frac{1}{2}\left(\frac{\partial\widetilde{u}_i}{\partial x_j}+\frac{\partial\widetilde{u}_j}{\partial x_i}\right) \tag{3.11}$$

where $\mu_T$ is the turbulent/eddy viscosity, $S$ is the strain rate tensor and $\delta_{ij}$ is the Kronecker delta. The turbulent heat transport is commonly approximated using the classical Reynolds analogy:

$$\overline{\rho}\widetilde{u_j''h''} = -\kappa_T \frac{\partial \widetilde{T}}{\partial x_j} \tag{3.12}$$

where $\kappa_T$ is the turbulent/eddy thermal heat conductivity. Application of the eddy viscosity hypothesis allows the dynamic viscosity $\mu$ in the viscous stress tensor in Equation 3.2 and Equation 3.3 to be replaced by the sum of a laminar and turbulent component:

$$\mu = \mu_L + \mu_T \tag{3.13}$$

where $\mu_L$ is the laminar viscosity, which can be computed using Sutherland's law. In a similar fashion, according to the Reynolds analogy, a laminar and turbulent component can be used to replace the thermal conductivity $\kappa$ in Equation 3.3:

$$\kappa = \kappa_L + \kappa_T = c_p \left( \frac{\mu_L}{Pr_L} + \frac{\mu_T}{Pr_T} \right) \tag{3.14}$$

where $\kappa_L$ is the laminar thermal heat conductivity and $Pr_L$ and $Pr_T$ are the laminar and turbulent Prandtl numbers, respectively.

Thermodynamic closure can be achieved by assuming a calorically perfect gas. The following relations then hold: $\overline{p} = (\gamma - 1)\,\overline{\rho}\left(\widetilde{e_0} - \frac{1}{2}\widetilde{u}_i\widetilde{u}_i\right)$, $\widetilde{T} = \overline{p}/\overline{\rho}R$ and $c_p = \gamma R/(\gamma - 1)$.

The eddy viscosity hypothesis is very attractive from an engineering perspective because it only requires the determination of the eddy viscosity. The two turbulence models implemented in the SU2 suite are the one equation Spalart-Allmaras (SA) model and the two equation $k - \omega$ Shear Stress Transport (SST) model. The SA model is effectively a low Reynolds number model and is not suitable for compressible flow unless the model is adapted. Turbulence closure in the present study will therefore be achieved with the $k - \omega$ SST model.

### 3.3.1. $k-\omega$ SST

In the present study turbulence closure will be achieved with Menter's [21] widely used $k-\omega$ Shear Stress Transport (SST) model. This is a two-equation model for the Reynolds/Favre-averaged turbulent kinetic energy and specific turbulence dissipation rate $\omega$. The model consists of a blend of the traditional high Reynolds number $k-\epsilon$ model which has been converted into the $k-\omega$ formulation, and the $k-\omega$ model by Wilcox. In this effort, the SST model attempts to merge the superior elements of both models. The $k-\omega$ SST model formulates the eddy viscosity as:

$$\mu_T = \frac{a_1 \overline{\rho}\widetilde{k}}{max\left(a_1 \widetilde{\omega}, \tilde{S}F_2\right)} \tag{3.15}$$

where $a_1$ is a model constant, $\tilde{S} = \sqrt{2\tilde{S}_{ij}\tilde{S}_{ij}}$ and $F_2$ is the second blending function. The $k-\omega$ SST model must be run with a suitable boundary layer spacing to allow for $y^+ \approx 1$ in order to prevent deterioration of the results. The values for the model constants and the form of the transport functions for the turbulent kinetic energy and specific turbulence dissipation rate, and the blending and auxiliary functions can be found in the paper by Menter [21].

# Chapter 4

# Adjoint-Based Shape Optimisation

This chapter presents the governing equations of the adjoint optimisation method, with emphasis on the discrete approach. A brief discussion on the adjoint solver, surface parametrisation and mesh deformation methods is also presented.

The treatment in this chapter is intentionally brief as its purpose is to introduce the reader to the discrete adjoint method, emphasising its simplicity when viewed in the context of linear algebra. A detailed discussion on this topic is too exhaustive and is clearly beyond the scope of this research. For a more detailed presentation the reader is encouraged to closely examine the work of Giles and Pierce [22] and Pini [23].

All vectors presented in this chapter are conventionally assumed as column vectors.

## 4.1. Governing Equations

The goal of fluid dynamic design optimisation is to minimise a cost function $J$ that for most practical purposes has a non-linear dependence on a set of discrete state variables. Pini et al. [24] elaborate that in fluid dynamic problems, the cost function generally depends on a vector of physical and geometrical design variables $\boldsymbol{\alpha}$, state variables $\mathbf{u}$ and mesh points $\mathbf{X}$. The state variables represent all the conserved flow variables that arise from the approximate solution of the flow governing equations at the discrete mesh

points. The state variables are dependent on the physical and geometrical variables while the mesh points solely depend on the geometrical parameters. For most practical purposes however, the physical variables can be considered as fixed and can therefore be omitted from the design variable vector. The cost function can then be written as:

$$J = J\left[\mathbf{u}\left(\boldsymbol{\alpha}\right), \mathbf{X}\left(\boldsymbol{\alpha}\right)\right] \tag{4.1}$$

The state variables $\mathbf{u}$ are constrained to satisfy the flow governing equations presented in section 3.3 for an arbitrary choice of $\boldsymbol{\alpha}$. The residuals of the governing equations $\mathbf{R}$ can be symbolically written as:

$$\mathbf{R}\left[\mathbf{u}\left(\boldsymbol{\alpha}\right), \mathbf{X}\left(\boldsymbol{\alpha}\right)\right] = 0 \tag{4.2}$$

Notice that Equation 4.2 can be considered an equality constraint for the fluid dynamic design optimisation. The equality constraint must hold for any choice of $\boldsymbol{\alpha}$ and therefore the derivative of $\mathbf{R}$ must also be null at all times. The derivative of $\mathbf{R}$ can be expressed as:

$$\frac{d\mathbf{R}}{d\boldsymbol{\alpha}} = \frac{\partial \mathbf{R}}{\partial \mathbf{u}} \frac{\partial \mathbf{u}}{\partial \boldsymbol{\alpha}} + \frac{\partial \mathbf{R}}{\partial \mathbf{X}} \frac{\partial \mathbf{X}}{\partial \boldsymbol{\alpha}} = 0 \tag{4.3}$$

In fluid dynamic design optimisation the main question of interest is; what is the perturbation in the cost function due to a perturbation in the geometry and thus in the flow field? The gradient of the cost function with respect to the geometrical design variables reads:

$$\frac{dJ}{d\boldsymbol{\alpha}} = \frac{\partial J}{\partial \mathbf{u}} \frac{\partial \mathbf{u}}{\partial \boldsymbol{\alpha}} + \frac{\partial J}{\partial \mathbf{X}} \frac{\partial \mathbf{X}}{\partial \boldsymbol{\alpha}} \tag{4.4}$$

The aim is to evaluate Equation 4.4 while the state variables are constraint to satisfy Equation 4.2. The direct sensitivity of the cost function to perturbations in the state variables is easy to evaluate. The computation of the direct sensitivity of the state variables to perturbations in the geometrical variables is usually a very demanding and computationally inefficient

operation. A straightforward but computationally prohibitive method to compute $\partial\mathbf{u}/\partial\boldsymbol{\alpha}$ is the finite difference method. In an alternative attempt, the same sensitivity is obtained by resolving the so called primal form of the optimisation given by:

$$\left(\frac{\partial\mathbf{R}}{\partial\mathbf{u}}\right)\left(\frac{\partial\mathbf{u}}{\partial\boldsymbol{\alpha}}\right) = -\left(\frac{\partial\mathbf{R}}{\partial\mathbf{X}}\frac{\partial\mathbf{X}}{\partial\boldsymbol{\alpha}}\right) \tag{4.5}$$

The primal form however requires considerable CPU memory utilisation as a series of N decoupled linear systems has to be solved, where N represents the number of columns in the term $(\partial R/\partial\mathbf{X})(\partial\mathbf{X}/\partial\boldsymbol{\alpha})$ which is equal to the number of geometrical design variables. Solving the primal form can be avoided by rewriting Equation 4.5 as:

$$\frac{\partial\mathbf{u}}{\partial\boldsymbol{\alpha}} = -\left(\frac{\partial\mathbf{R}}{\partial\mathbf{u}}\right)^{-1}\left(\frac{\partial\mathbf{R}}{\partial\mathbf{X}}\frac{\partial\mathbf{X}}{\partial\boldsymbol{\alpha}}\right) \tag{4.6}$$

and by plugging the previous equation in Equation 4.4. The result is that the cost function gradient with respect to the geometrical design variables can be expressed as:

$$\frac{dJ}{d\boldsymbol{\alpha}} = -\frac{\partial J}{\partial\mathbf{u}}\left(\frac{\partial\mathbf{R}}{\partial\mathbf{u}}\right)^{-1}\left(\frac{\partial\mathbf{R}}{\partial\mathbf{X}}\frac{\partial\mathbf{X}}{\partial\boldsymbol{\alpha}}\right) + \frac{\partial J}{\partial\mathbf{X}}\frac{\partial\mathbf{X}}{\partial\boldsymbol{\alpha}} \tag{4.7}$$

The term $(-\partial J/\partial\mathbf{u})(\partial\mathbf{R}/\partial\mathbf{u})^{-1}$ is called the adjoint variables vector $\mathbf{v}$. Consequently the adjoint variables vector can be determined by resolving the so called linear adjoint system:

$$\left(\frac{\partial\mathbf{R}}{\partial\mathbf{u}}\right)^{\mathsf{T}}\mathbf{v} = -\left(\frac{\partial J}{\partial\mathbf{u}}\right)^{\mathsf{T}} \tag{4.8}$$

which is the dual form of the primal system and represents the adjoint equations in discrete form. The gradient of the cost function with respect to the design variables is finally expressed as:

$$\left(\frac{dJ}{d\boldsymbol{\alpha}}\right)^{\mathsf{T}} = \left(\frac{\partial \mathbf{X}}{\partial \boldsymbol{\alpha}}\right)^{\mathsf{T}} \left[\left(\frac{\partial J}{\partial \mathbf{X}}\right)^{\mathsf{T}} + \left(\frac{\partial \mathbf{R}}{\partial \mathbf{X}}\right)^{\mathsf{T}} \mathbf{v}\right] \tag{4.9}$$

It is noteworthy to point out that unlike the primal form, computation of the dual form is independent of the number of geometrical design variables. The choice is to solve either the primal form given by Equation 4.5 or the dual (adjoint) form given by Equation 4.8. For a single geometrical design variable there would be no benefit nor disadvantage in using the adjoint approach. For multiple geometrical design variables however, the primal form has to be solved for each design variable whereas the dual form only has to be solved once. This results in the adjoint approach to be computationally much more efficient.

In addition to the flow governing equations, engineering design applications often also require a set of constraints to be satisfied. Some constraints can be geometric while others may depend on the flow variables. Geometric constrains are easily incorporated by altering the search direction for the design variables to ensure that the geometric constraints are satisfied. Constraints that depend on the flow variables require the value of the constraint function and its linear sensitivity to the design variables. The latter requires another adjoint calculation; the addition of more flow-based constraints would require even more adjoint calculations. This type of constraint therefore undermines the computational benefit of the adjoint approach and should therefore be kept to a minimum.

## 4.2. Adjoint Solver

The evaluation of the cost function gradient with respect to the design variables, defined by Equation 4.9, involves several Jacobian matrices that have to be build. This requires a numerical gradient calculation method; the Algorithmic Differentiation (AD) method is first formally described. This method is implemented in the SU2 computational suite adopted in the present study.

The AD technique exploits the fact that every function specified by a computer program is a concatenation of elementary arithmetic operations. By applying the chain rule to this concatenation, derivatives of arbitrary order can be precisely determined with computer accuracy. The AD technique can be used in forward or reverse mode; the difference lies in the direction of traversing the chain rule derivatives.

The step-by-step procedure of calculating the cost function gradient with respect to the design variables, as defined by Equation 4.9, can be briefly summarised as:

1. The first step is to calculate the adjoint variables vector $\mathbf{v}$ appearing in the last term in Equation 4.9. The adjoint vector is obtained by solving Equation 4.8 which has the form $\mathbf{Av} = \mathbf{b}$, where $\mathbf{A} = (\partial \mathbf{R}/\partial \mathbf{u})^{\mathrm{T}}$ and $\mathbf{b} = -(\partial J/\partial \mathbf{u})^{\mathrm{T}}$. In the present study the iterative flexible generalised minimum residual (FGMRES) solver is adopted. This type of matrix-free solver does not require the explicit evaluation of the Jacobian $(\partial \mathbf{R}/\partial \mathbf{u})$, but it only calculates the product of $(\partial \mathbf{R}/\partial \mathbf{u})^{\mathrm{T}}\mathbf{v}$ at each iteration. The FGMRES method utilises the AD technique presented above in reverse mode to construct $(\partial \mathbf{R}/\partial \mathbf{u})^{\mathrm{T}}$ and $-(\partial J/\partial \mathbf{u})^{\mathrm{T}}$.

2. The second step is to calculate the gradient of the cost function with respect to the entire set of mesh points, given by the term in brackets Equation 4.9. This term is calculated by separately differentiating the numerical procedures that implement the functional $J(\mathbf{X})$ and $\mathbf{R}(\mathbf{X})$ using the AD technique in reverse mode. The transposed derivative of the functional $\mathbf{R}(\mathbf{X})$ is then multiplied with the adjoint variables vector and summed with the transposed derivative of $J(\mathbf{X})$.

3. The last step is to calculate the rate of mesh perturbation for a change in the design variables, given by the first term in parentheses in Equation 4.9, and to multiply its transpose with the gradient obtained in the previous step. The mesh perturbation gradient is obtained by differentiation of the mesh deformation equations, which are presented in section 4.4, using the AD formalism in reverse mode.

## 4.3. Surface Parametrisation

A critical aspect of automated fluid dynamic design of turbomachinery is the selection of an appropriate shape parametrisation method. The parametrisation method is key to ensure robustness and design flexibility of the entire optimisation process. Vitale et al. [25] report that the use of surface nodes as design variables may lead to discontinuous solutions. An alternate method must therefore be considered; Samareh [26, 27] performed a survey of shape parametrisation techniques and states that the Computer-Aided Design (CAD) and the Free Form Deformation (FFD) methods have the desirable characteristics of being efficient, compact and suitable for complex configurations.

In a CAD-based method, the blade shape is parametrised with non-uniform rational basis spline (NURBS) curves and the position of the control points is derived from geometrical characteristics of the blade. The advantage of this method is that large shape changes can be achieved and that blade geometrical constraints can be easily implemented. However, parametrisation of existing complex shapes is still a challenging task and the shapes created are not always good enough for automated mesh generation tools. The implementation of a CAD-based method in the computational tool used in the present study would be time consuming and costly and is therefore not considered ideal.

In a FFD-based method, a parallelogram control lattice is constructed around (a part of) the blade surface and is deformed using a tensor product of Bernstein basis polynomials. The embedded surface mesh points are deformed in a continuous way by moving only the control points of the lattice. The FFD approach only allows small to medium geometry changes. The advantage of parametrising the mesh on the surface is that the topology stays fixed throughout the optimisation; hence, the mesh can be deformed automatically. According to Anand et al. [28], the FFD-based method also offers a high degree of flexibility, but makes it hard to satisfy geometrical constraints. The geometrical constraints could be imposed by adapting the lattice to indirectly satisfy the geometrical constraints. The appealing fea-

tures of the FFD technique make it ideal for the present work.

## 4.4. Mesh Deformation

In the course of the optimisation, changes are made to the blade surface and therefore the mesh must be regenerated or deformed accordingly. Deforming a mesh tends to be substantially cheaper and more convenient than to regenerate it.

### 4.4.1. Surface Deformation

The control points $\mathbf{P}_{m,n}$ of the FFD control lattice can be displaced to continuously deform the embedded surface mesh points $\mathbf{X}_s$. The control points are therefore chosen as design variables, i.e. $\boldsymbol{\alpha} = \mathbf{P}_{m,n}$. The coordinates of the nodes on the deformed surface for the $d^{th}$ optimisation step are given by:

$$\mathbf{X}_s^d = \mathbf{X}_s^{d-1} + \Delta\mathbf{X}_s^d \tag{4.10}$$

The displacement of the surface nodes embedded in the control lattice can be expressed as a linear combination of lattice control points $\mathbf{P}_{m,n}$ and Berstein polynomials $B_m$ as:

$$\Delta\mathbf{X}_s^d = \sum_{m=0}^{k}\sum_{n=0}^{l} B_m^k\left(y_p\right) B_n^l\left(y_q\right)\left(\mathbf{P}_{m,n}^d - \mathbf{P}_{m,n}^{d-1}\right) \tag{4.11}$$

where $y_p$ is the local coordinate of $\mathbf{X}_s$ with respect to the control lattice in the $p^{th}$ direction, $B_m^k$ is the $m^{th}$ Bernstein polynomial in the $p^{th}$ direction and k represents the FFD degree in the $p^{th}$ direction.

### 4.4.2. Volume Deformation

The mesh deformation algorithm implemented in SU2 is based on a spring analogy method proposed by Dwight [29]. In this approach, the mesh is modelled as an elastic solid using the equations of linear elasticity. If the surface deformation $\Delta\mathbf{X}_s$ is imposed as a Dirichlet boundary condition in the equations of linear elasticity , the mesh deformation $\Delta\mathbf{X}$ can be determined by solving the linear system (Vitale [30]):

$$\mathbf{K}\Delta\mathbf{X} = \mathbf{T}\Delta\mathbf{X}_s \tag{4.12}$$

where $\mathbf{K}$ is a stiffness matrix and $\mathbf{T}$ is a projection matrix which re-orders $\Delta\mathbf{X}_s$ in accordance with $\mathbf{X}$. The coordinates of the mesh points for the $d^{th}$ optimisation step are then given by:

$$\mathbf{X}^d = \mathbf{X}^{d-1} + \Delta\mathbf{X}^d \tag{4.13}$$

A significant advantage of this approach is that diverse features required in practise can be readily and simply realised in a manner consistent with the model of the mesh as an elastic body (Dwight [29]). However, large surface variations can possibly produce unacceptable meshes due to the fixed topology. In this case the mesh must be regenerated manually during the optimisation.

An overview of the mesh deformation method is illustrated in Figure 4.1. This type of method is included in the SU2 computational suite used in the present study.

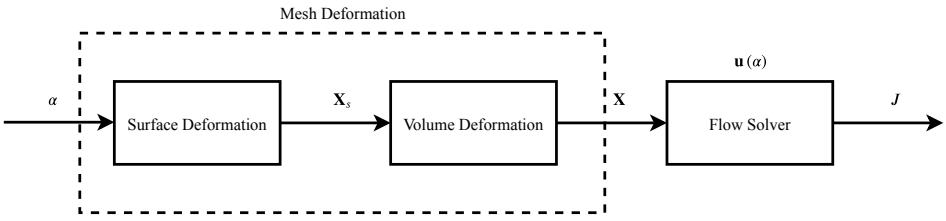


Figure 4.1: Formal representation of the mesh deformation method based on the equations of linear elasticity. This method is implemented in the SU2 computational suite adopted in the present study.

## 4.5. Design Optimisation Chain

An overview of the automated design optimisation chain is visualised in Figure 4.2. This optimisation framework is implemented in the SU2 computational suite adopted in the present study.

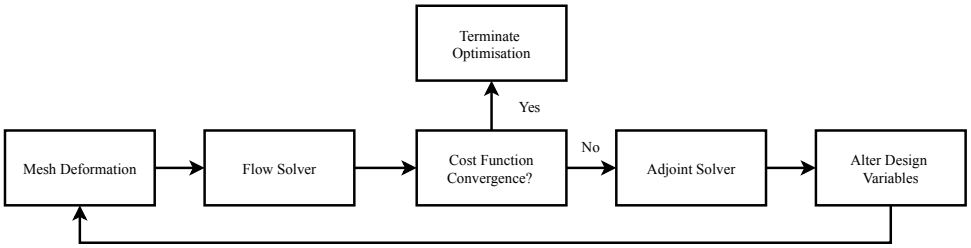


Figure 4.2: Formal representation of the automated adjoint-based design optimisation chain. This framework is implemented in the SU2 computational suite adopted in the present study.

# Chapter 5

# Methodology

This chapter presents an extensive description of the numerical setup and the loss breakdown method. The computational tool adopted in the present study is also briefly discussed.

## 5.1. Numerical Setup

The RANS-based discrete adjoint optimisation framework discussed in chapter 4 is now applied to improve the performance of the stator vane shown in Figure 5.2A. The supersonic stator vane is designed to operate with a high pressure ratio at design point and is employed in the first turbine stage of a 1MN-class gas generator cycle type rocket engine. The operating conditions are listed in Table 5.1 but can not be disclosed due to confidentiality reasons. The compressibility factor is unity and heat transfer effects are neglected.

| $p_{01}$ | $T_{01}$ | $p_2$ |
|---|---|---|
| $p_{01_{ref}}$ | $T_{01_{ref}}$ | $p_{2_{ref}}$ |

Table 5.1: Inlet stagnation pressure and temperature, and outlet pressure for the design optimisation.

| $\dot{m}$ | $\alpha_2$ | $M_2$ |
|---|---|---|
| $\dot{m}_{ref}$ | $\alpha_{2_{ref}}$ | $M_{2_{ref}}$ |

Table 5.2: Average target values for the mass flow rate, outlet Mach number and outlet flow angle $\alpha_2$.

### 5.1.1. Computational Tool

The computational tool utilised throughout the present work is the open-source software SU2 which is extensively described by Economon et al. [31]. SU2 is conceived for solving multi-physics PDEs and PDE-constrained optimisation problems using unstructured meshes. The tool leverages on an optimisation framework that incorporates a RANS discrete adjoint solver. The flow and the adjoint solver can be run on parallel CPU architectures, making the SU2 optimisation framework highly suited for systematic investigations aimed at defining best practises for turbomachinery design. The platform has been extended for turbomachinery applications by the Propulsion & Power group from the faculty of Aerospace Engineering at the University of Technology in Delft.

### 5.1.2. Flow Solver

The RANS equations discussed in section 3.3 are solved with the SU2 flow solver in order to obtain numerical flow solutions of the supersonic stator vane. Thermodynamic closure is achieved by assuming a calorically perfect gas, which is a valid approximation considering that the compressibility factor is unity, while turbulence closure is achieved by the two-equation $k-\omega$ SST model discussed in subsection 3.3.1. The laminar viscosity is determined using Sutherland's law and the laminar Prandtl number is assumed to be constant.

The flow solver is based on a finite volume method for spatial integration whereas in the present study the temporal integration is achieved through an implicit Euler method with a fixed Courant-Friedrichs-Lewy number of 10. The convective fluxes are discretised using a second-order accurate classic upwind Roe scheme and spurious oscillations due to shocks and discontinuities are avoided by the van Albada slope limiter. The viscous fluxes are determined using the weighted least square method. The $k-\omega$ SST equations are solved using an upwind scheme with a first-order reconstruction. The flow solver utilises the FGMRES method, which is an

efficient iterative matrix-free solver. The performance of this solver is further enhanced using the Lower-Upper Symmetric Gauss-Seidel (LUSGS) preconditioner.

Non-reflecting boundary conditions are implemented allowing calculations to be performed on truncated domains without generation of non-physical reflections at the far-field boundaries, leading to improved accuracy and computational efficiency because the mesh can be made much smaller (Giles [32]). The number of iterations is set to result in a reduction of about four orders in the residuals of the conserved quantities in the governing equations.

All the relevant settings of the SU2 flow solver are listed in Table 5.3.

| | **Setting** | |
|---|---|---|
| **Governing Equations** | RANS | |
| **Turbulence Modelling** | $k-\omega$ SST | |
| | **Flow** | **Turbulence** |
| **Time Discretisation** | Euler Implicit | |
| **Spatial Gradients** | Weighted Least Squares | |
| **CFL** | 10 | 1 |
| **Convective Numerical Method** | Upwind Roe | Scalar Upwind |
| **Spatial Integration** | 2nd order | 1st order |
| **Slope Limiter** | Van Albada Edge | Venkatakrishnan |
| | **Setting** | |
| **Linear Solver** | FGMRES | |
| **Preconditioner** | LUSGS | |

Table 5.3: An overview of all the relevant settings of the SU2 flow solver.

### 5.1.3. Adjoint Solver

The adjoint equations discussed in section 4.1 are solved with the SU2 adjoint solver. The adjoint solver also utilises the FGMRES method with the LUSGS preconditioner. The gradient components are efficiently constructed by exploiting the AD technique in reverse mode, preliminarily to evaluate the adjoint system, then to obtain the terms appearing in the derivative of the cost function with the design variables. All the relevant settings of the SU2 adjoint solver are listed in Table 5.4.

| | **Setting** |
|---|---|
| **Adjoint Solver** | FGMRES |
| **Preconditioner** | LUSGS |

Table 5.4: An overview of all the relevant settings of the SU2 adjoint solver

### 5.1.4. Optimisation

The optimisation process aims at minimising the entropy generation coefficient $\xi_s$ while achieving the average target flow quantities listed in Table 5.2. The values of the average target flow quantities cannot be disclosed due to confidentiality reasons. The cost function in the adjoint equations presented in chapter 4 is the entropy generation coefficient, i.e. $J = \xi_s$. The entropy generation coefficient is defined as:

$$\xi_s = \frac{s_2 - s_1}{\frac{u_{2s}^2}{T_{01}}} \tag{5.1}$$

where $u_{2s} = \sqrt{2\,(h_{01} - h_{2s})}$ is the isentropic downstream velocity, also referred to as the spouting velocity. The thermodynamic quantities required to calculate the entropy generation coefficient and the isentropic downstream velocity are obtained using the mixed-out averaging procedure.

### Constraints

An optimisation of the entire stator vane is very challenging due to the performance, manufacturing and thermomechanical constraints. To satisfy the mass flow rate criteria for a given working fluid and for the upstream stagnation conditions listed in Table 5.1, the throat area must remain unaltered to keep the corrected flow per unit area constant. In addition, the stator vane is built layer by layer in the axial direction using additive manufacturing; this imposes a limit on the maximum surface angle upstream of the throat. At last, a minimum trailing edge thickness is enforced by thermomechanical constraints.

As a result, the only parts of the stator vane surface that can be changed are the leading edge, pressure surface and the supersonic suction surface. It is hypothesized that the former two parts of the stator vane surface do not largely influence the overall flow because they mostly operate in the subsonic regime. The focus is therefore turned to improve the performance of the supersonic suction surface. In this way, the mass flow rate, the manufacturing and thermomechanical requirements can be indirectly satisfied. The hypothesis is proven by inspection of the values of the entropy generation gradient computed all along the blade surface. The results are shown in Figure 5.1 and indicate that only changes in the supersonic suction surface significantly impact the entropy generation.

Since the throat and trailing edge shapes are fixed, the overall passage area ratio is also fixed. It is therefore expected that the outlet flow angle and the outlet Mach number will not significantly change. These performance constraints will therefore not be directly imposed on the optimisation. If the outlet flow angle and Mach number constraints are not satisfied after a preliminary optimisation, the optimisation problem will be reformulated to include them.

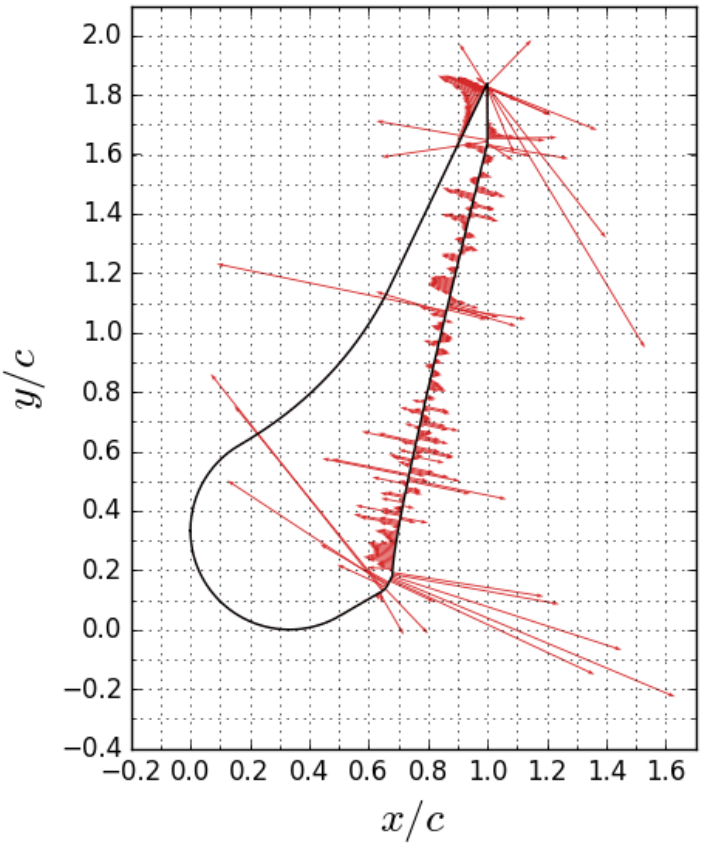


Figure 5.1: Gradient vectors of the entropy generation coefficient with respect to the surface points of the supersonic stator. The axial location, pitchwise location and axial chord are given by $x$, $y$ and $c$, respectively. Note that the gradients on the leading edge, pressure surface and subsonic suction surface are very small.

### Surface Parametrisation

The FFD method discussed in section 4.3 is applied to parametrise the supersonic suction surface of the stator vane. The control lattice is defined by $k = 8$ degrees in the $p^{th}$ direction and $l = 4$ degrees in the $q^{th}$ direction, as shown in Figure 5.2B. The total number of control variables is 45. The control points are bound to move perpendicular to the axial direction.

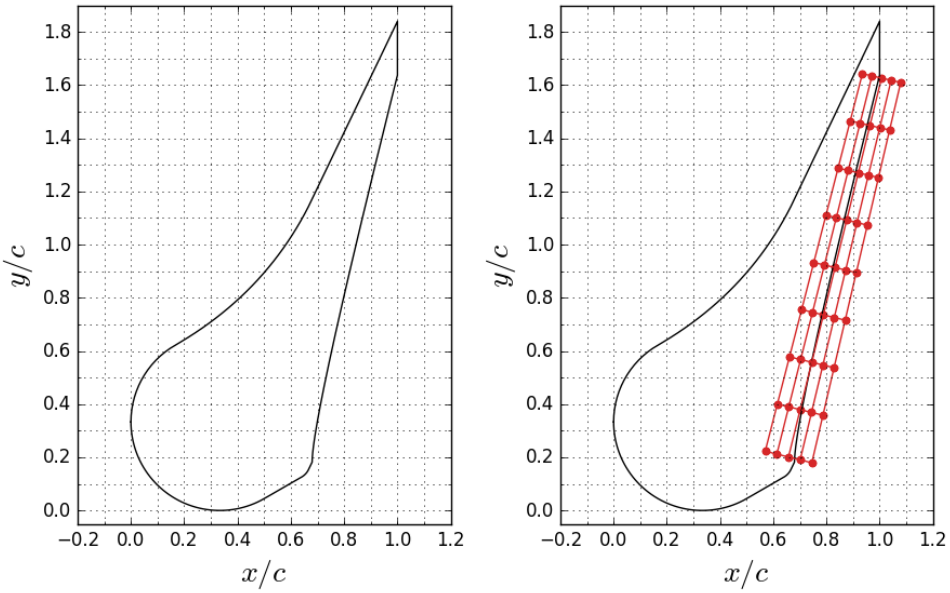


(A) (B)

Figure 5.2: (A) Geometry of the supersonic stator vane. (B) FFD parametrisation of the supersonic suction surface. The red dots are the design variables of the FFD method. The axial location, pitchwise location and axial chord are given by $x$, $y$ and $c$, respectively.

### Mesh Deformation

Changes made to the blade surface are propagated through the mesh using the spring analogy method described in section 4.4.

### Optimisation Problem

The unconstrained optimisation of the supersonic suction surface of the stator vane is formulated as:

$$\underset{\boldsymbol{\alpha}}{\text{minimise}} \quad J(\boldsymbol{\alpha}) = \xi_s(\boldsymbol{\alpha})$$

where the vector of geometrical design variables $\boldsymbol{\alpha}$ is defined by the set of 45 control points shown in Figure 5.2B. Recall that the performance constraints listed in Table 5.2, and the manufacturing and thermomechanical constraints are indirectly satisfied.

**Optimiser**

The gradient-based optimisation framework implemented in SU2 uses a Sequential Least Squares Programming (SLSQP) algorithm to minimise the cost function. This algorithm uses the Quasi-Newton method with a Broyden-Fletcher-Goldfarb-Shanno update for the Hessian of the cost function. Convergence of the optimisation is achieved by satisfying the Karush-Kuhn-Tucker (KKT) conditions with a tolerance of $1 \times 10^{-6}$. The cost function is scaled with $1 \times 10^{-6}$ and the maximum number of optimisation iterations is set to 50. All the relevant settings of the SU2 optimiser are listed in Table 5.5.

| | **Setting** |
|---|---|
| **Optimiser** | SLSQP |
| **Convergence Criteria** | KKT |
| **Convergence Tolerance** | $1 \times 10^{-6}$ |
| **Scaling of Cost Function** | $1 \times 10^{-6}$ |
| **Maximum Number of Iterations** | 50 |

Table 5.5: An overview of all the relevant settings of the SU2 optimiser.

## 5.2. Loss Breakdown Method

There are various ways to define loss coefficients that measure loss creation in turbines; a comparison by Brown [33] shows that values of the energy loss coefficient change the least with the Mach number. In the present study losses are determined using the energy loss coefficient $\xi \approx 1-\eta$ which is proposed in the experimental study by Mee et al. [1], where $\eta$ is the primary efficiency. The efficiency parameter $\eta$ is a ratio of the attained kinetic energy to the isentropic kinetic energy at the downstream plane. In terms of the enthalpy $h$ the energy loss coefficient for a turbine blade row may be written as:

$$\xi \approx 1 - \eta = 1 - \frac{h_{02} - h_2}{h_{02} - h_{2s}} \tag{5.2}$$

where $\xi$ is the energy loss coefficient and the subscript $s$ refers to a quantity that is obtained in an isentropic process.

The two-dimensional loss components discussed in section 2.2 can be expressed in terms of the energy loss coefficient defined by Equation 5.2. An overview of the loss breakdown method for supersonic blades developed in the present study is illustrated in Figure 5.3 and a detailed explanation on the different loss components and the total loss is given in the following subsections. For subsonic and transonic blades, an overview of the methodology can be found in Appendix A.

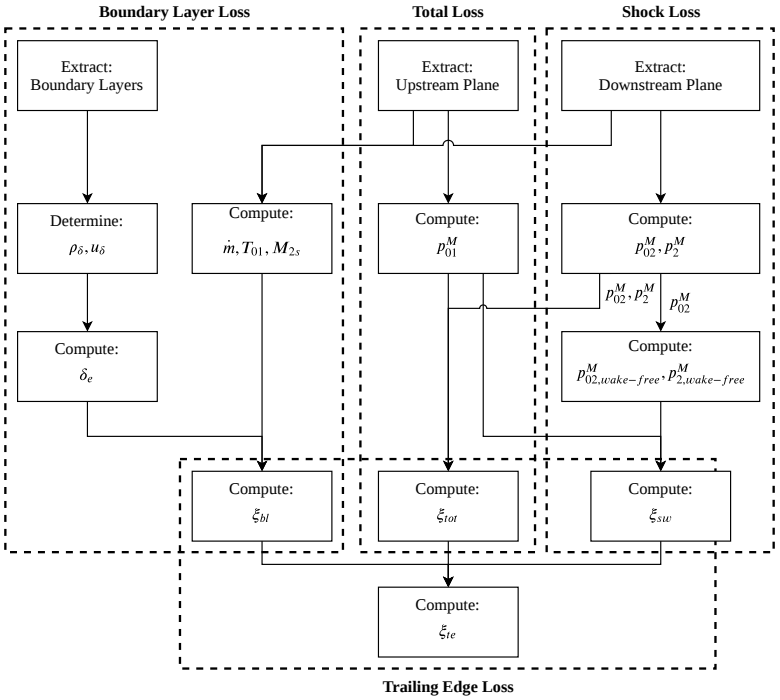


Figure 5.3: Overview of the two-dimensional loss breakdown method for supersonic blades adopted in the present study, where the superscript $M$ indicates a mass-weighted average. The loss components and the total loss are expressed in terms of the energy loss coefficient $\xi$ and it is assumed that the working fluid is fixed and behaves like a calorically perfect gas. Stations 1 and 2 refer to the upstream and downstream plane, respectively.

### 5.2.1. Boundary Layer Loss

The boundary layer loss can be quantified in terms of the energy loss coefficient by relating it to the mechanical energy that is converted into heat in the layers. An estimate of this dissipation can be obtained by measuring the defect between the mechanical energy in the actual layers and those that would be present at free-stream conditions. This is done using the kinetic energy thickness $\delta_e$ which is defined as:

$$\delta_e = \int_0^{\delta} \frac{\rho u}{\rho_\delta u_\delta^3} \left(u_\delta^2 - u^2\right) dy \tag{5.3}$$

The rate of kinetic energy loss in the boundary layer $\dot{e}_{k_{bl}}$ is then given by:

$$\dot{e}_{k_{bl}} = 0.5 \rho_\delta \delta_e u_\delta^3 \tag{5.4}$$

If the flow expanded isentropically from upstream conditions to the downstream conditions, the kinetic energy flux at the downstream plane would be:

$$\dot{e}_{k_{2s}} = \dot{m} \left(h_{02} - h_{2s}\right) \tag{5.5}$$

Noting that for a calorically perfect gas $h = c_p T$ and that for isentropic flow $T_{01} = T_{02}$, Equation 5.5 can be rewritten as:

$$\dot{e}_{k_{2s}} = \dot{m} c_p T_{01} \left[1 - \left(1 + \frac{\gamma - 1}{2} M_{2s}\right)^{-1}\right] \tag{5.6}$$

where $M_{2s}$ is the isentropic exit Mach number. The boundary layer energy loss coefficient $\xi_{bl}$ can now be determined as the ratio of Equation 5.4 and Equation 5.6 as (Mee et al. [34]):

$$\xi_{bl} = \frac{0.5 \rho_\delta \delta_e u_\delta^3}{\dot{m} c_p T_{01} \left[1 - \left(1 + \frac{\gamma-1}{2} M_{2s}\right)^{-1}\right]} \tag{5.7}$$

In the present study the layers are extracted at 0.75 $l/l_{max}$ and 0.9 $l/l_{max}$ of the pressure and suction surface, respectively, where the curvilinear abscissa $l$ is measured from the leading edge. The height used for the boundary layer extraction is estimated from a preliminary CFD calculation. The boundary layer extraction on the baseline profile is illustrated in Figure 5.4.

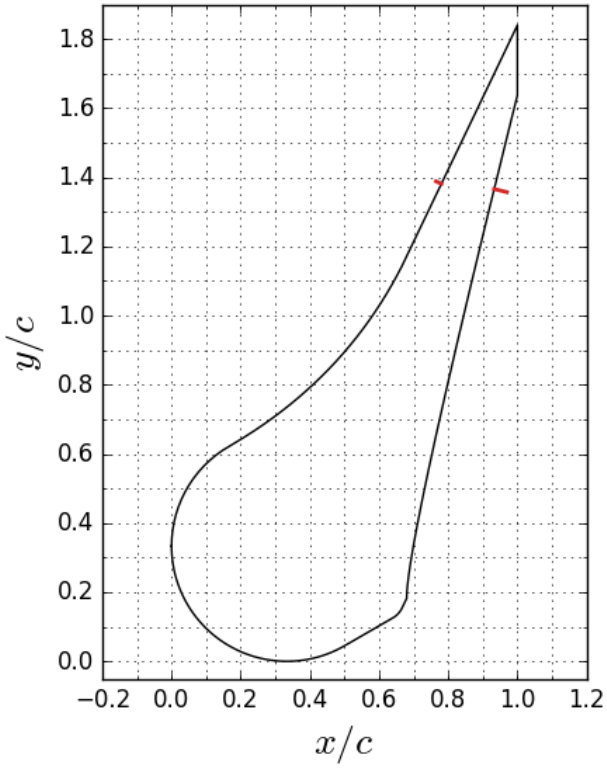


Figure 5.4: Visualisation of the boundary layer (red) extraction at 0.75 $l/l_{max}$ and 0.9 $l/l_{max}$ of the pressure and suction surface, respectively, where the curvilinear abscissa $l$ is measured from the leading edge. The axial location, pitchwise location and axial chord are given by $x$, $y$ and $c$, respectively.

According to Mee et al. [34], the contribution of the pressure surface boundary layer to the overall boundary layer loss is negligible because it is one order of magnitude smaller than the suction surface layer. Here, it is not considered mostly because of ease of implementation.

### 5.2.2. Shock loss

The shock loss component is evaluated in terms of the energy loss coefficient by investigating the stagnation pressure deficit in the wake-free regions at the downstream plane. Recall that for an isentropic process $T_{01} = T_{02}$ and also:

$$\frac{T}{T_0} = \left(\frac{p}{p_0}\right)^{\frac{\gamma-1}{\gamma}} \tag{5.8}$$

By combining these two properties of an isentropic flow, and noting that for a calorically perfect gas $h = c_p T$, the energy loss coefficient given by Equation 5.2 can be rewritten as (Oldfield et al. [35]):

$$\xi_{sw} = 1 - \frac{1 - \left(\frac{p_2}{p_{02}}\right)^{\frac{\gamma-1}{\gamma}}}{1 - \left(\frac{p_2}{p_{01}}\right)^{\frac{\gamma-1}{\gamma}}} \tag{5.9}$$

where $\xi_{sw}$ is the shock wave energy loss coefficient. The pressure and stagnation pressures in Equation 5.9 must be estimated in a way that they represent the shock loss. To develop one comprehensive method for subsonic, transonic and supersonic flows is quite cumbersome, and therefore two different approaches are proposed below.

#### Subsonic and Transonic Flows

In subsonic and transonic flows an estimate of the pressure and the stagnation pressures in Equation 5.9 is obtained by extracting a streamline that is not affected by the boundary layer and the trailing edge loss, a so called inviscid streamline. This type of streamline is set to pass through the center of the throat section. This crude approximation holds quite well for subsonic and transonic flows, as will be demonstrated in subsection 5.2.5. Figure 5.5 illustrates the inviscid streamline for the LS89 turbine stator vane operating under subsonic and transonic operating conditions.

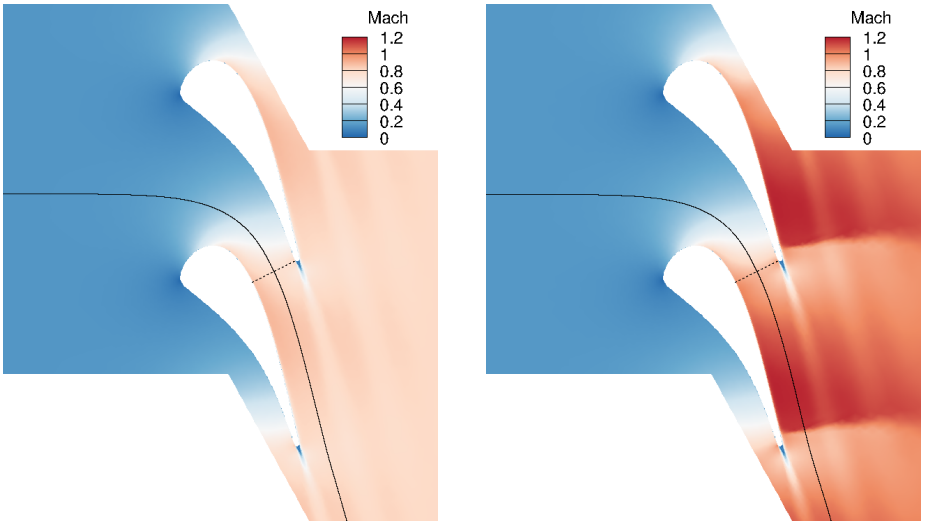


(A) $M_{2s}$ = 0.81 (B) $M_{2s}$ = 1.04

Figure 5.5: Visualisation of the inviscid streamline (solid line) for the LS89 blade for subsonic (A) and transonic (B) operating conditions. The inviscid streamline passes through the center of the throat (dotted line). The pressure and stagnation pressure along the inviscid streamline are used for the calculation of the shock loss.

### Supersonic Flows

The inviscid streamline method described above does not work for supersonic flows because the strong shocks cause significant deflection of the streamline, often resulting it to end near or inside a wake. Therefore, for supersonic flows, a mass-weighted average for the downstream static pressure and stagnation pressure is calculated in the wake-free regions. The wake-free regions are crudely defined as the downstream locations in which the local stagnation pressure is larger than the mass-weighted average of the entire downstream plane. The upstream stagnation pressure can be calculated as a mass-weighted average for the entire upstream plane.

The wake-free region obtained with this method is highlighted in Figure 5.6, which shows the pitchwise stagnation pressure at the downstream plane of the supersonic stator vane investigated in the present study. Figure 5.7 shows the stagnation pressure contour of the same stator vane. A manual inspection of the wake-free region in Figure 5.7 reveals that the proposed method for supersonic flow, demonstrated in Figure 5.6, is fairly accurate.

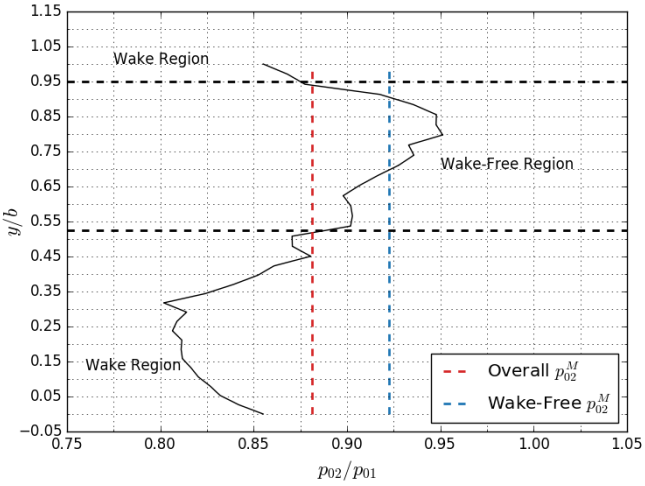


Figure 5.6: Definition of the downstream wake-free region for the supersonic stator vane investigated in the present study under nominal operating conditions, where $y$ is the pitchwise location, $b$ is the blade pitch and the subscript M represents a mass-weighted average.

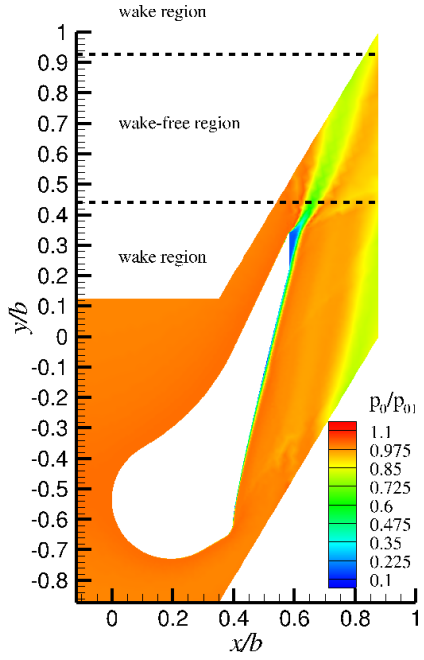


Figure 5.7: Manual inspection of the wake-free region using the stagnation pressure contour of the supersonic stator vane studied in the present study under nominal operating conditions, where $y$ is the pitchwise location and $b$ is the blade pitch.

### 5.2.3. Trailing Edge Loss

The trailing edge loss is computed in terms of the energy loss coeffient as the difference between the total loss, and the individual loss contributions originating from the boundary layers and the shocks. The trailing edge loss is given by:

$$\xi_{te} = \xi_{tot} - \xi_{bl} - \xi_{sw} \tag{5.10}$$

where $\xi_{te}$ and $\xi_{tot}$ are the trailing edge energy loss coefficient and the total energy loss coefficient, respectively.

### 5.2.4. Total Loss

The total loss is determined in a similar fashion as the shock loss. However, the mass-weighted average for the downstream static pressure and stagnation pressure are now calculated for the entire downstream plane so that they represent all the losses occurring in the blade passage.

### 5.2.5. Validation

The loss breakdown procedure is validated with experimental results produced by Mee et al. [1]. The experimental results are shown in Figure 2.4. The geometry of the transonic turbine stator blade used in the experimental study is not available in literature and therefore the transonic LS89 turbine blade will be used for validation. The cascade of LS89 turbine blades has been studied extensively at the von Karman Institute for Fluid Dynamics and has gained a lot of popularity in the recent years as a validation case (Arts et al. [36]). A comparison will be made between the energy loss components of the LS89 blade, obtained using the loss breakdown method for subsonic and transonic blades described above, and the experimental data shown in Figure 2.4. Numerical measurements of the loss components for the LS89 blade at a $Re$ of about $3 \times 10^6$ are shown in Figure 5.8 whereas

Mach contours for different $M_{2s}$ are shown in Figure 5.9.

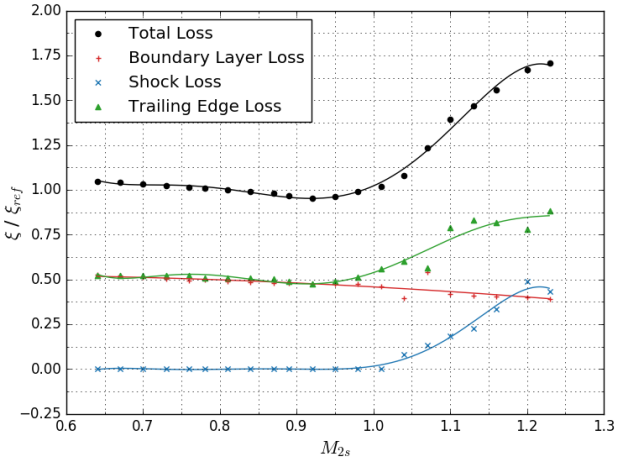


Figure 5.8: Numerical measurements of the variation of energy loss coefficient $\xi$ with isentropic exit Mach number $M_{2s}$ for the transonic LS89 turbine blade at a Reynolds number of approximately $3 \times 10^6$. The reference loss coefficient is the total loss coefficient under nominal operating conditions of $M_{2s}$ = 0.81.

There is a strong agreement in the loss trends of the experimental data shown in Figure 2.4 and the numerical data shown in Figure 5.8. Notice that the experimental data is shown with the exit Mach number, whereas the numerical data is shown with the isentropic exit Mach number $M_{2s}$.
The boundary layer and shock loss component, and the overall loss display nearly identical behaviour. The trailing edge loss trends are also very similar, except for sonic conditions. It is noted that for these conditions the method applied for calculating the trailing edge loss is influenced by the appearance of shocks. However, for subsonic Mach numbers shock waves are absent and there the trailing edge loss trends are comparable. The numerical results also suggest the same trends for the supersonic regime.
The trends are also in agreement with a more recent numerical study to loss generation in transonic turbines by Duan et al. [37]. In this study the losses are presented in terms of entropy generation, but still display identical behaviour for all the loss components except for the trailing edge component. This difference is arguably due to the different definition for

the trailing edge loss adopted in the present study.

The numerical trends of the overall loss and the loss components are in agreement with the experimental data and therefore the loss breakdown method is considered to be validated.

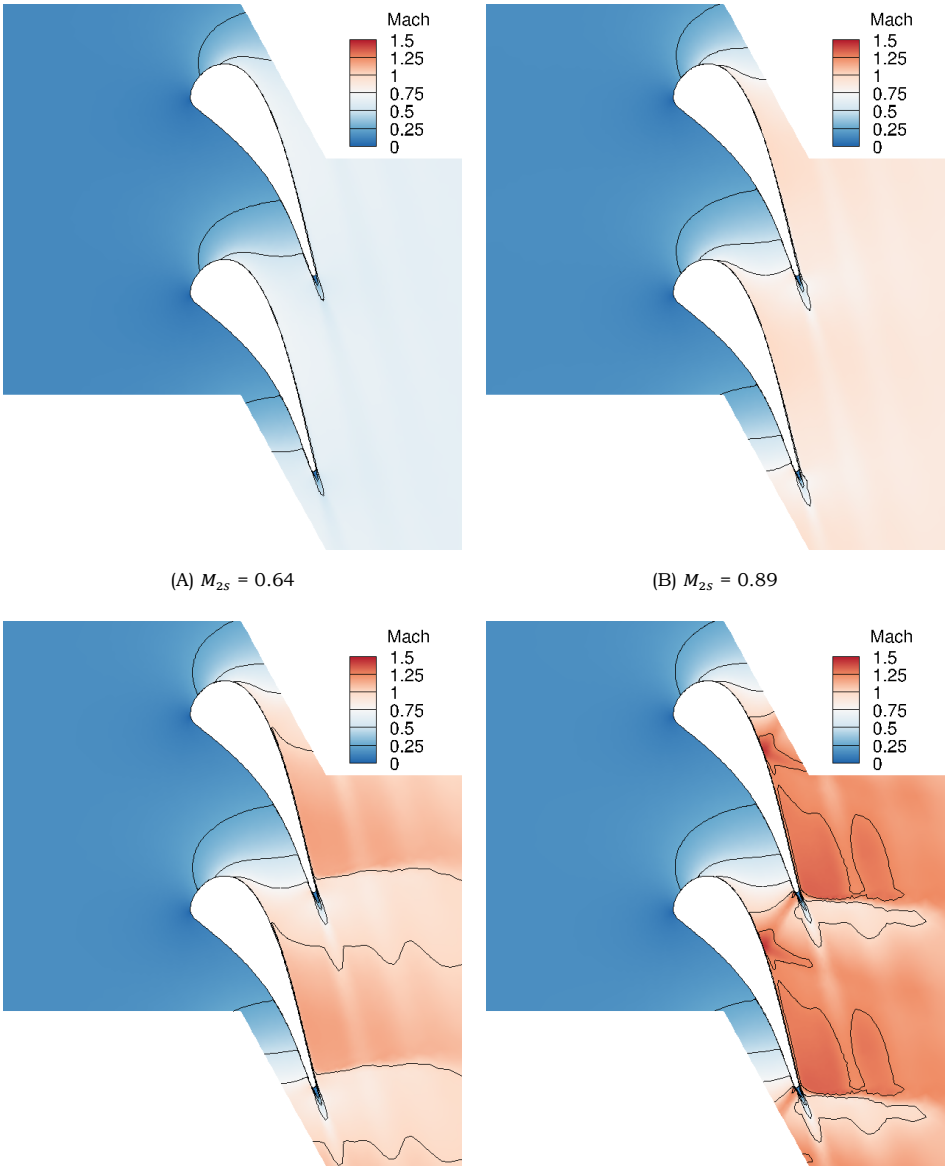


(A) $M_{2s}$ = 0.64 (B) $M_{2s}$ = 0.89

(C) $M_{2s}$ = 1.04 (D) $M_{2s}$ = 1.2

Figure 5.9: Mach contours of the transonic LS89 turbine stator blade for different isentropic exit Mach numbers $M_{2s}$.

# Chapter 6

# Results

This chapter presents the results of the shape optimisation defined in chapter 5. The baseline and optimised designs are investigated and compared using the loss breakdown method developed in chapter 5. In addition, this chapter provides a mesh sensitivity study, validation of the adjoint method and an investigation of the excitation on the adjacent blade row.

## 6.1. Mesh Sensitivity

Meshing of the supersonic stator vane is performed using the robust in-house unstructured UMG2 code. Turbulence effects are modelled using the $k-\omega$ SST model discussed in subsection 3.3.1 and therefore the mesh is set to maintain a maximum $y^+$ value of unity on the blade surface. The non-reflective upstream and downstream boundaries are located at 0.2 and 0.5 axial chords away from the blade surface, respectively. The hybrid mesh is composed of triangular elements in the far-field and quadrilateral elements near the blade surface. Figure 6.1 shows the sensitivity of the stagnation pressure loss coefficient on the mesh size. The stagnation pressure loss coefficient $Y$ for turbines is given by:

$$Y = \frac{p_{01} - p_{02}}{p_{02} - p_2} \tag{6.1}$$

where the pressure and stagnation pressures are obtained using the mixed-out averaging procedure. The final mesh has $63 \times 10^3$ cells and the stagnation pressure loss coefficient is within 0.5 percentage points of the finest

mesh value, which is deemed to be acceptable for optimisation purposes.

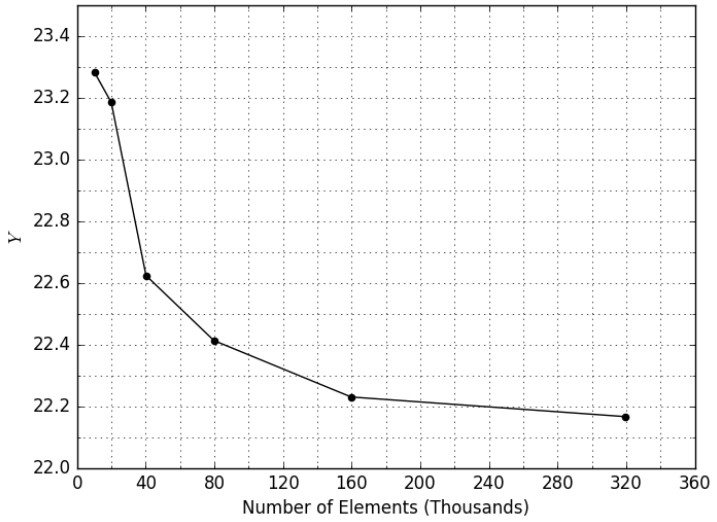


Figure 6.1: Mesh sensitivity to the stagnation pressure loss coefficient $Y$. The final mesh has $63 \times 10^3$ cells and the stagnation pressure loss coefficient is within 0.5 percentage points of the finest mesh value.

## 6.2. Gradient Validation

The gradients obtained from the discrete adjoint method are validated with a first-order reconstruction of the forward finite difference scheme and a corresponding step size of $1 \times 10^{-3}$. Figure 6.2 shows a scatter plot of the gradients of entropy generation obtained using the discrete and finite difference method. Note that many points are piled up in the origin of the plot because the corresponding gradients are nearly zero. There is a very good agreement between both methods, except for some control points that are located near the trailing edge of the blade surface. It is well-known that sharp edges have a large impact on the overall flow and loss performance of stator vanes. Palacios et al. [38] point out that from a mathematical point of view, the evaluation of gradients in such non-smooth regions is difficult for complex geometries. The gradients in these regions are therefore less accurate and this also explains why there is relatively less agreement

between the different methods near the trailing edge.

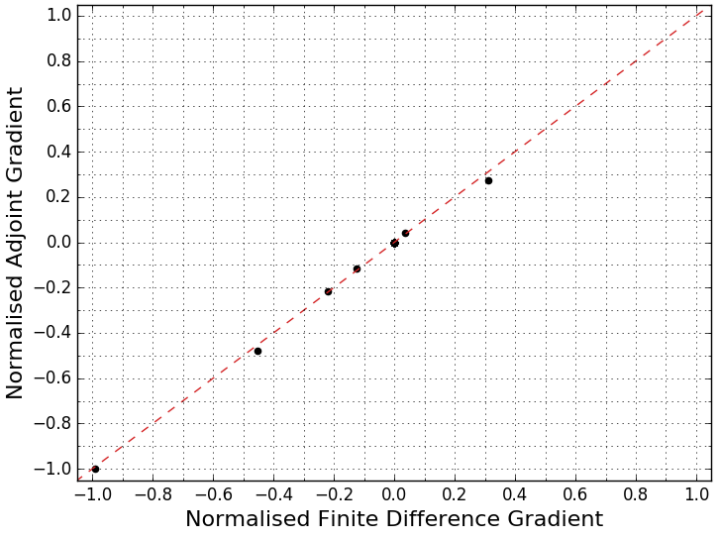


Figure 6.2: Gradient validation of the discrete adjoint method with a first-order reconstruction of the forward finite difference scheme and a corresponding step size of $1 \times 10^{-3}$. The gradients are normalised with the largest absolute value of all gradients.

## 6.3. Optimisation

The convergence history of the optimisation problem defined in subsection 5.1.4 is shown in Figure 6.3. The optimisation processes have converged within 49 iterations. The entropy generation coefficient is reduced by about 6% and the equality performance constraints are also satisfied, as listed in Table 6.1. In addition, the pitchwise outlet pressure non-uniformity in terms of the area-weighted standard mean deviation is reduced by 6%.

| $\dot{m}/\dot{m}_{ref}$ | $\alpha_2/\alpha_{2_{ref}}$ | $M_2/M_{2_{ref}}$ |
|---|---|---|
| 1.00 | 1.00 | 1.00 |

Table 6.1: Average values for the mass flow rate, outlet Mach number and the outlet flow angle of the optimised stator vane.

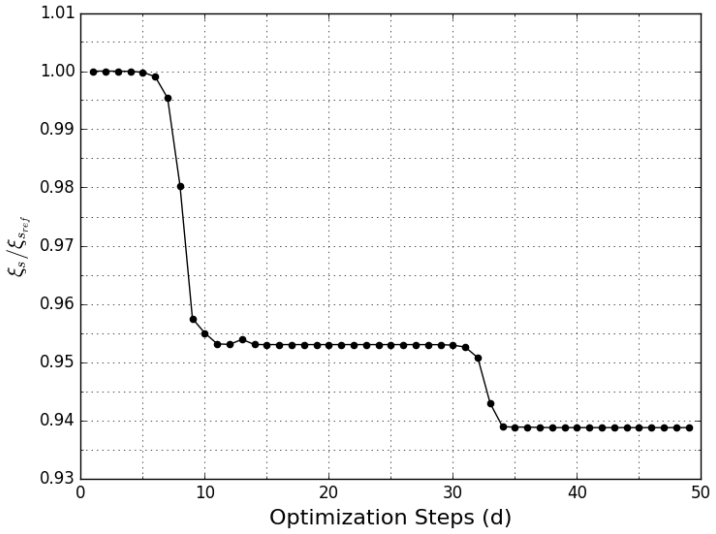


Figure 6.3: Convergence history of the cost function, i.e. the entropy generation coefficient $\xi_s$. The reference value is the $\xi_s$ at the first optimisation step.

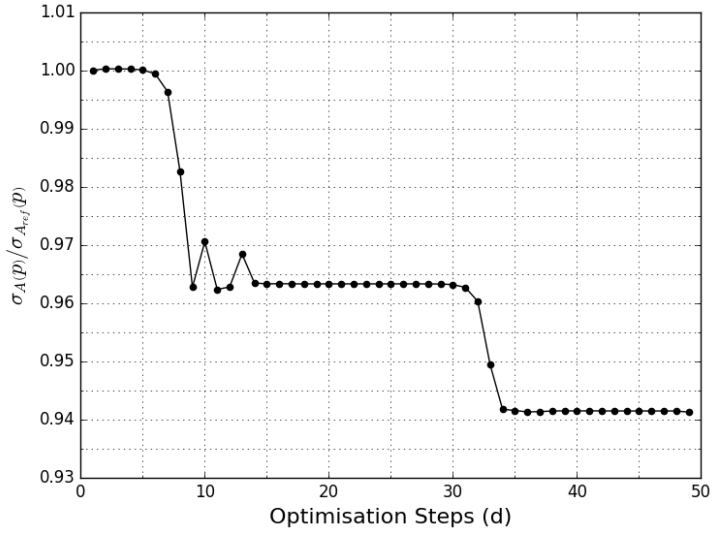


Figure 6.4: Area-weighted standard mean deviation $\sigma_A$ of the pitchwise outlet pressure for different design iterations. The reference value is the $\sigma_A$ at the first optimisation step.

The baseline and optimised stator vane geometries are displayed in Figure 6.5. The optimisation procedures lead to a curved supersonic suction surface with a concave shape in the throat region and a convex shape towards the trailing edge. This produces a variation of the local passage area ratio, without altering the overall passage area ratio. The maximum change between geometry of the baseline and optimised stator vane is in the order of 0.04 axial chords and is within the machining accuracy of the additive layer manufacturing method.

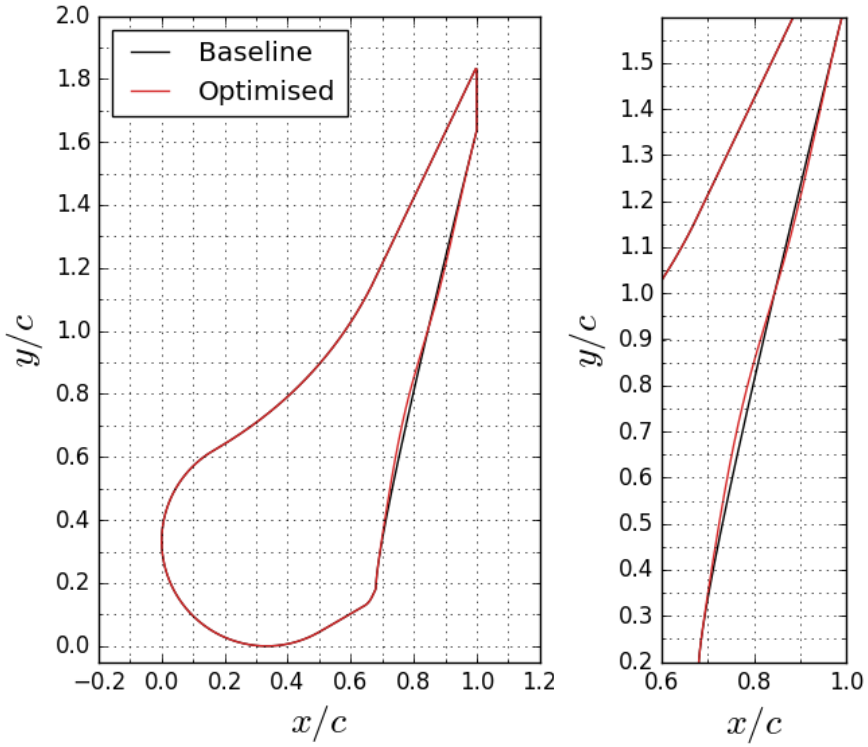


(A) Entire stator vane (B) Supersonic suction surface

Figure 6.5: Baseline and optimised stator vane geometries. The optimised suction surface is more concave in the throat region and more convex towards the trailing edge. The order of the geometry change is about 0.04 axial chords. The axial location, pitchwise location and axial chord are given by $x$, $y$ and $c$, respectively.

### 6.3.1. Assessment of Fluid-Dynamic Performance

The variation of the energy loss components with the design iterations is illustrated in Figure 6.6. The most significant reduction is observed in the shock loss component, whereas the components of boundary layer and trailing edge loss remain nearly constant. In turn, the overall performance improvement can be mainly attributed to the reduction of the shock loss.

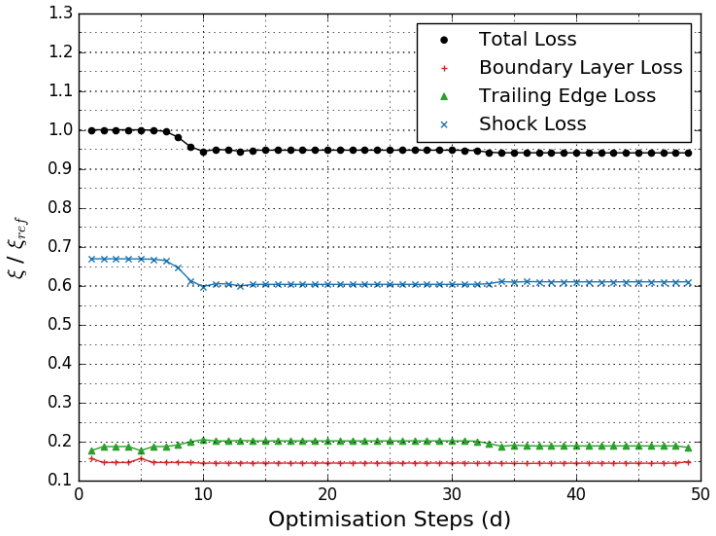


Figure 6.6: Variation of the loss components in terms of the energy loss coefficient $\xi$ with the respect to the design iterations. It is observed that the optimiser mainly acts on the shock loss. The reference loss coefficient is the total loss coefficient calculated at the first design step.

#### Boundary Layer Loss

As visible in Figure 6.6, it is safe to say that the boundary layer loss of the baseline and optimised stator vane is identical. This assumption is supported by Figure 6.7, which shows the pressure and suction surface boundary layers of the baseline and optimised stator vane.

There is no visible difference between the pressure surface layer of the baseline and optimised stator vane. This is as expected because no changes have been made to the pressure surface of the stator vane. Recall that

measurements by Mee et al. [34] indicated that the contribution of the pressure surface layer to the total boundary layer loss is negligible because the pressure surface layer is an order of magnitude smaller than the suction surface layer. These findings are supported by the present study; the pressure surface loss of the optimised stator vane is two orders of magnitude smaller than the suction surface loss.

The boundary layer edge velocity of the suction surface layer of the optimised stator vane is seen to be slightly larger than that of the baseline suction surface layer. The suction surface boundary layer edge properties of the baseline and optimised stator vane are listed in Table 6.2. Recalling that the mechanical energy dissipated in the layers is given by Equation 5.4, it can be assumed that the overall change in the suction surface boundary layer loss is negligible.

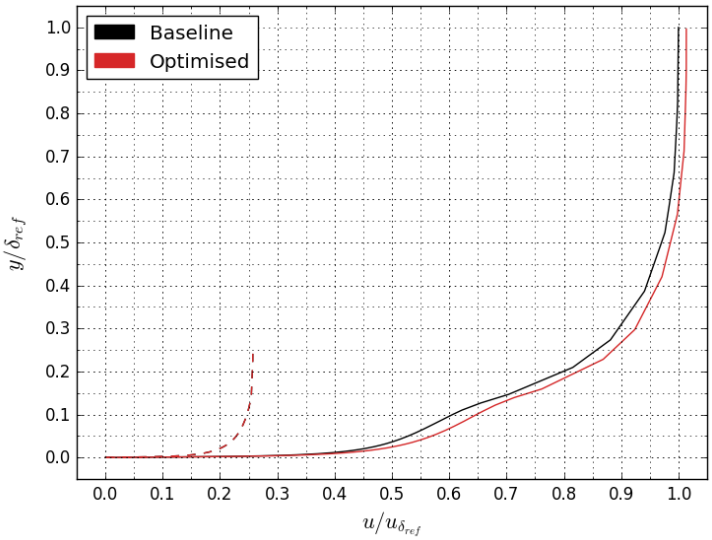


Figure 6.7: Pressure (dotted line) and suction (solid line) boundary layers of the baseline and optimised stator vane. The layers are extracted at 0.75 $l/l_{max}$ and 0.9 $l/l_{max}$ of the pressure and suction surface, respectively, where the curvilinear abscissa $l$ is measured from the leading edge. The reference values represent the suction surface of the baseline design.

| | $\rho_\delta/\rho_{ref}$ | $u_\delta/u_{ref}$ | $\delta_e/\delta_{ref}$ |
|---|---|---|---|
| Baseline | 1.00 | 1.00 | 0.107 |
| Optimised | 0.96 | 1.03 | 0.101 |

Table 6.2: Suction surface boundary layer edge properties of the baseline and optimised stator vane.

**Shock Loss**

From Figure 6.9, which shows a numerical Schlieren flow visualisation, it becomes visible that the oblique shock generated on the supersonic suction surface is weakened in the optimised design. This is a direct consequence of changing the local passage area ratio; the area-Mach relation relates the Mach number at any location to the ratio of the local passage area to the throat area. The higher passage area ratio of the optimised stator vane immediately downstream of the throat leads to a larger acceleration of the flow, consequently increasing the boundary layer losses. This effect can be seen in Figure 6.8 for $0 < l/l_{max} < 0.34$, which shows a comparison of the supersonic suction surface loading between the baseline and optimised stator vane. As the flow continues to expand in the concave region of the optimised stator vane, it is slightly turned into itself. This leads to a reduced flow acceleration and consequently a lower Mach number upstream of the oblique shock. This effect is illustrated in Figure 6.8 for $0.34 < l/l_{max} < 0.6$. The result is that the concave part produces a smaller loss in stagnation pressure compared to the straight suction surface with an oblique shock wave with a larger upstream Mach number. The increase of the boundary layer loss does not compensate for the decreased shock loss. The net effect is a less pronounced flow acceleration on the supersonic suction surface and consequently a weaker oblique shock wave. This is also illustrated in Figure 6.10, which shows the Mach contours of the baseline and optimised stator vane.

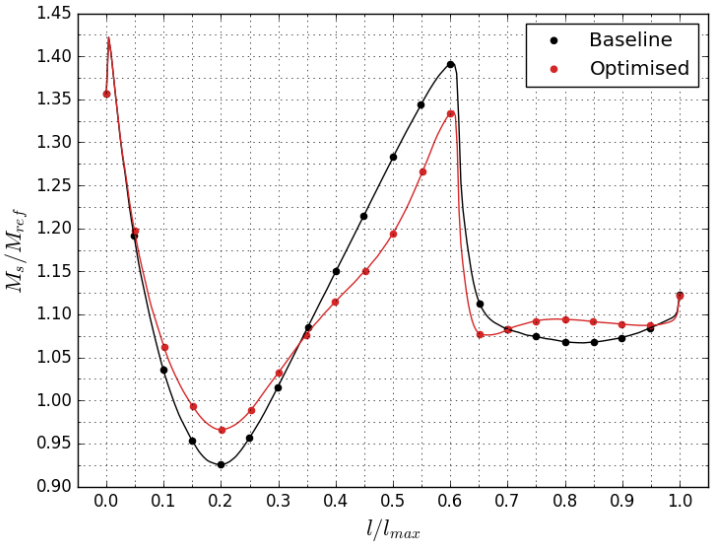


Figure 6.8: A comparison of the supersonic suction surface loading in terms of the surface isentropic Mach number $M_s$ between the baseline and optimised stator vane. The curvilinear abscissa $l$ is measured from the throat. The reference value represents the average target value for the outlet Mach number.

### Trailing Edge Loss

The change in trailing edge loss between the baseline and optimised stator vane is also negligible. Recall from subsection 2.2.3 that the trailing edge loss is generated by the low base pressure acting on the trailing edge, mixing of the momentum contained in the boundary layers and the combined blockage of the boundary layers and the trailing edge. In the present study the trailing edge shape is fixed. In addition, it can be seen in Figure 6.10 that the flow in the vicinity of the trailing edge is very similar for the baseline and optimised design. The boundary layer density and velocity profiles towards the trailing edge are also very similar for the baseline and optimised stator vane, as listed in Table 6.2. Therefore, the trailing edge loss remains relatively constant.

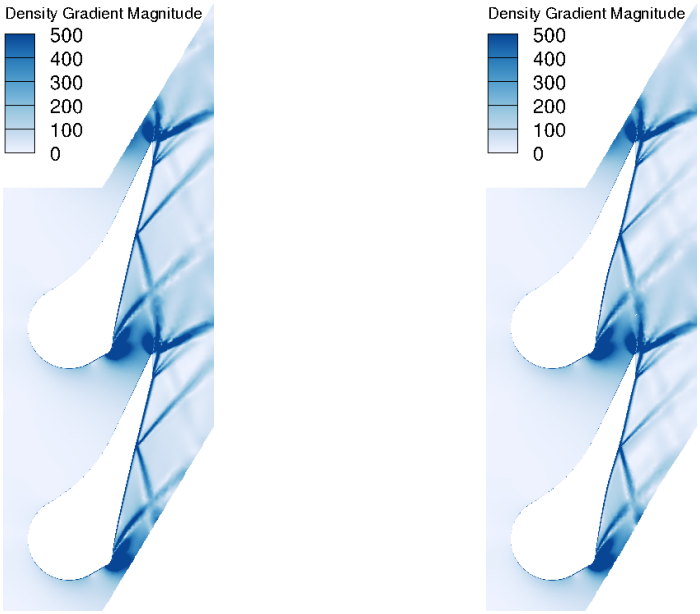


(A) Baseline (B) Optimised

Figure 6.9: Numerical Schlieren visualisation of the baseline and optimised supersonic stator vane by means of the density gradient magnitude.

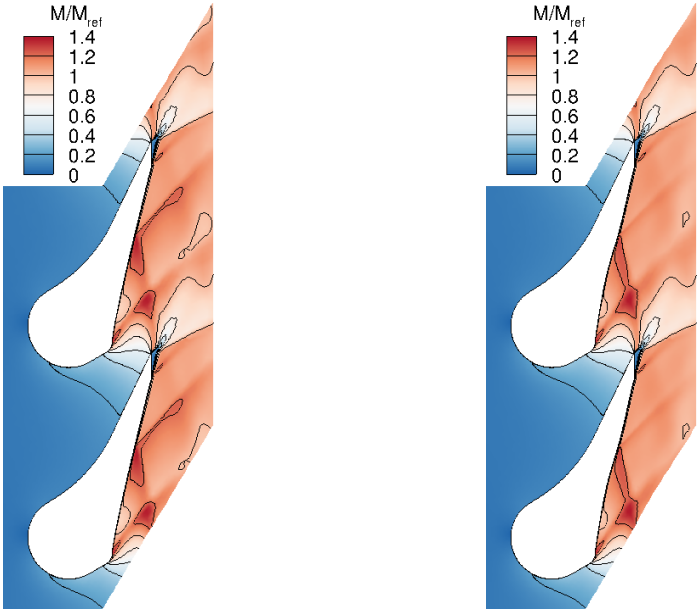


(A) Baseline (B) Optimised

Figure 6.10: Mach contours of the baseline and optimised stator vane. The reference value represents the average target value for the outlet Mach number.

**Flow Non-Uniformity**

The interaction between the mechanical and aerodynamic forces acting on a structure (aeroelasticity) can give rise to various types of vibrations that can lead to mechanical failure. There are several aeroelastic problems that are of interest for turbomachinery engineers, but the present study is particularly concerned with the forced response caused by the stator-rotor interaction.

Forced responses are intrinsically linked to the excitation forces that originate from the inherent unsteady nature of the flow within turbines. A spatial non-uniform distribution of pressure in a stator row is seen as temporal disturbance in the adjacent rotor row. The temporal disturbances cause a periodic forcing on the rotor blades with an amplitude and frequency that are based on the magnitude of the non-uniformities, and the number of stator blades and the rotational speed of the adjacent rotor blades, respectively. Forced response is a recurrent shortcoming in rocket engine turbines and its reduction can lead to a significant increase of the lifetime of the component.

Stator-rotor interaction effects can be limited by reducing the magnitude of the spatial pressure non-uniformities at the outlet of the stator row. Figure 6.4 shows the area-weighted standard mean deviation $\sigma_A$ of the pitchwise pressure at the stator outlet for different design iterations. It is observed that while the optimiser reduces the entropy generation coefficient, it also reduces the pressure non-uniformities at the stator outlet. As a result, it is expected that the optimised stator induces less excitation on the adjacent rotor blade compared to the baseline stator vane.

Figure 6.11 shows the pitchwise outlet pressure and Mach distributions of the baseline and optimised stator blade. It is observed that the outlet flow has become more uniform. This is a direct consequence of adopting the mixed-out averaging procedure for calculating the entropy generation coefficient; a more uniform outlet pressure and Mach distribution will lead to a smaller mixed-out entropy. Consequently, a more uniform outlet pressure and Mach distribution will result in a smaller entropy generation coeffi-

cient. Therefore, the optimiser indirectly acts on the outlet pressure and Mach distributions in order to reduce the entropy generation coefficient.

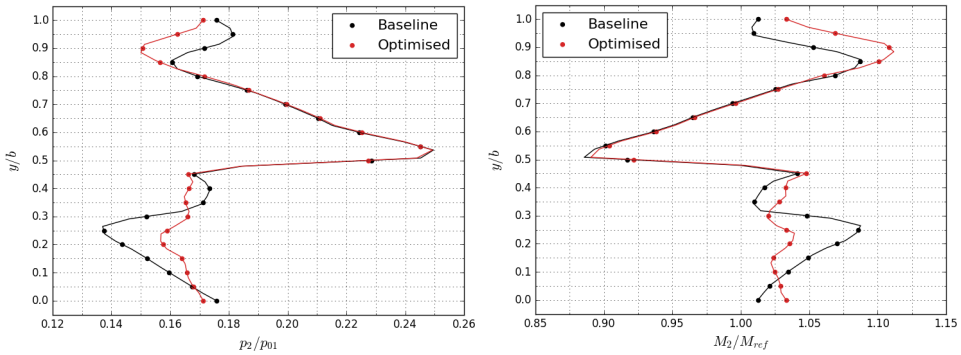


(A) (B)

Figure 6.11: Spanwise pressure (A) and Mach (B) distributions at the stator vane outlet of the baseline and optimised design, where $y$ and $b$ are the pitchwise location and the blade pitch, respectively. The reference Mach number represents the average target value for the outlet Mach number. It can be seen that the optimised stator has a more uniform outlet flow.

A significant change in the pressure and Mach non-uniformity is observed for $0.0 < y/b < 0.45$; this region is associated with the wake of the supersonic stator vane. This statement is confirmed by manual inspection of the wake/wake-free regions in Figure 6.12, which shows the normalised stagnation pressure contour of the optimised stator vane. This might seem unintuitive at first; a high pressure and low Mach number is expected in the wake region, however, the opposite is observed. This is a consequence of the strong trailing edge shock which is present in the free-stream flow and significantly increases the pressure and reduces the Mach number, so that the wake-free pressure and Mach number are higher and lower compared to the wake region, respectively. This effect is clearly visible in Figure 6.13, which shows the pressure and Mach contour of the optimised stator vane. The wake region is influenced by the complex shock structure observed in the flow field, as illustrated in Figure 6.9 and Figure 6.10. As a result, part of the free-stream flow ends up in the blade wake, as illustrated with the streamlines in Figure 6.12. The flow field within the wakes is thus influenced by the presence of the free-stream shock waves.

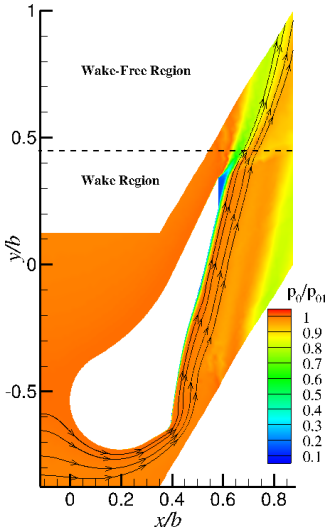


Figure 6.12: Normalised stagnation pressure contours with free-stream streamlines that end up in the stator vane wake. The stagnation pressure contours are normalised with the inlet stagnation pressure.

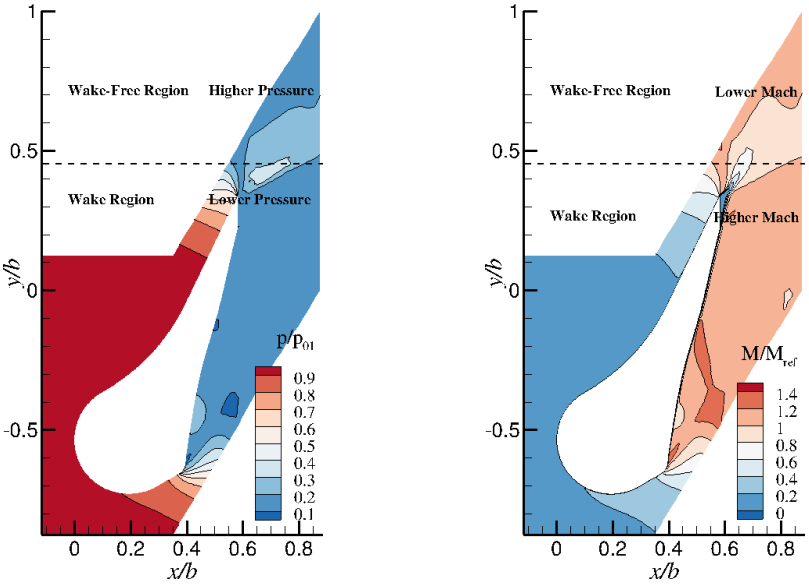


(A) (B)

Figure 6.13: Pressure (A) and Mach (B) contour of the optimised supersonic stator vane, where y, x and b are the pitchwise location, axial chord and pitch, respectively. The pitchwise location for the wake/wake-free region is obtained by manual inspection of Figure 6.12. The reference Mach number represents the average target value for the outlet Mach number.

## 6.4. Loss Trends

Figure 6.14 shows the individual loss components of the baseline and optimised stator vane for a range of $M_{2s}$. The trends of the loss components are similar for the baseline and optimised stator vane. In general, the boundary layer loss decreases monotonically with $M_{2s}$. The shock and trailing edge loss components display non-monotonic behaviour. The shock loss peaks near nominal conditions of $M_{2s}/M_{ref}$ = 1.06 and the inverse holds for the trailing edge loss. The total loss remains relatively constant and significantly increases for $M_{2s}/M_{ref}$ > 1.19.

In Appendix B the reader can find the variation of the loss components with the axial chord Reynolds number.

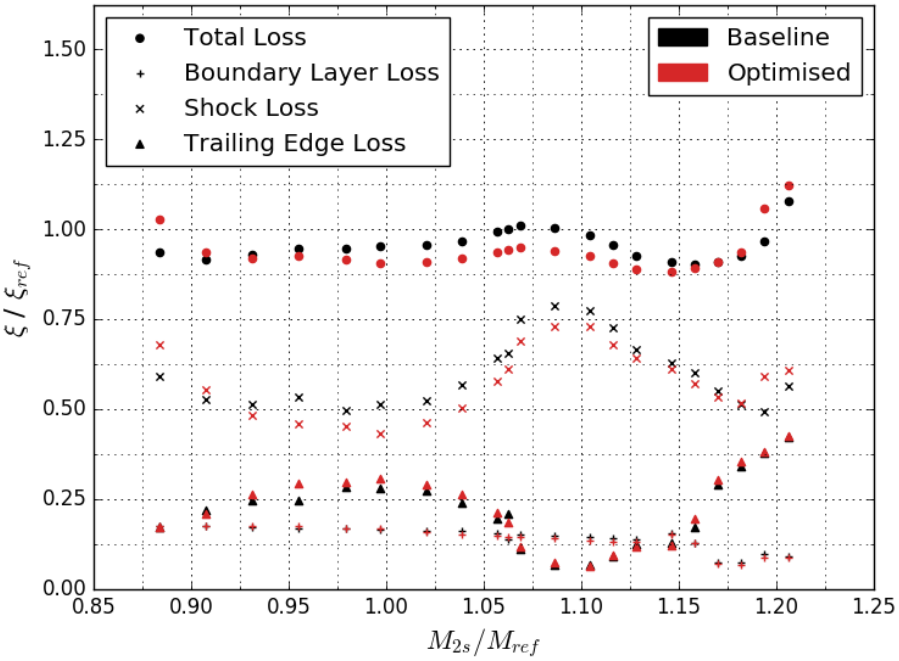


Figure 6.14: Numerical measurements of the variation of energy loss coefficients $\xi$ with isentropic exit Mach number $M_{2s}$ for the baseline and optimised stator vane. The reference loss coefficient represents the total loss coefficient of the baseline design under nominal operating conditions of $M_{2s}/M_{ref}$ = 1.06. The reference Mach number represents the average target value for the outlet Mach number.

### 6.4.1. Boundary Layer Loss

The variation of the boundary layer loss is shown in Figure 6.14. The boundary layer loss contribution to the total loss is relatively insignificant over the wide range of $M_{2s}$. It can be seen that the boundary layer loss decreases monotonically with $M_{2s}$ and the results indicate that the boundary layer loss will keep decreasing for $M_{2s}/M_{ref} > 1.19$. This observation can be elucidated with reference to the supersonic suction surface loading of the optimised stator vane depicted in Figure 6.15. It is seen that there exists a favourable pressure gradient for $l/l_{max} > 0.2$ until an oblique shock wave impinges on the suction surface. The effect of the favourable pressure gradient, whose length increases with $M_{2s}$, is to decrease the boundary layer thickness. However, the oblique shock wave also interacts with the suction surface boundary layer and gives rise to strong adverse pressure gradient which increases the boundary layer thickness. This impact outweighs the effect of the favourable pressure gradient decreasing the layer thickness. The combined effect is that the boundary layer thickness increases with $M_{2s}$. However, the momentum and kinetic energy thickness remain relatively constant with $M_{2s}$. This is visible in Figure 6.16, which shows the variation of the boundary layer thickness parameters with $M_{2s}$. Note that the ideal kinetic energy leaving the downstream plane increases with $M_{2s}$. Thus, recalling that the boundary layer energy loss coefficient involves the ratio of mechanical energy dissipated to the isentropic mechanical energy leaving the downstream plane, the net effect is that the boundary layer loss decreases with $M_{2s}$.

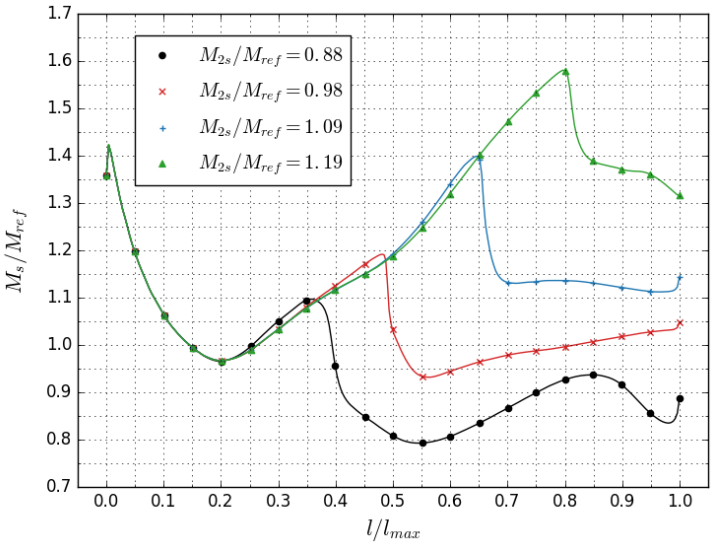


Figure 6.15: Suction surface isentropic Mach number $M_2$ distributions of the optimised stator vane for different isentropic exit Mach numbers $M_{2s}$. The reference Mach number represents the average target value for the outlet Mach number. The curvilinear abscissa $l$ is measured from the throat.

### 6.4.2. Shock Loss

The variation of the shock loss component is shown in Figure 6.14. The shock loss significantly contributes to the total loss and the results suggest that this contribution keeps increasing for $M_{2s}/M_{ref} > 1.19$. For the range of $M_{2s}$ shown in Figure 6.14, the shock loss displays non-monotonic behaviour. The shock loss trend can be explained by the shock structures that are observed in Figure 6.17, which show a numerical Schlieren visualisation for different $M_{2s}$. For $M_{2s}/M_{ref}$ = 0.88, as illustrated in Figure 6.17A, an oblique shock wave impinges on the supersonic suction surface close to the throat and is reflected. As $M_{2s}$ is increased, as depicted for $M_{2s}/M_{ref}$ = 0.98 in Figure 6.17B and for $M_{2s}/M_{ref}$ = 1.09 in Figure 6.17C, the oblique shocks move downstream along the suction surface and become less inclined. If $M_{2s}$ is increased even more, as illustrated for $M_{2s}/M_{ref}$ = 1.19 in Figure 6.17D, the oblique shocks move so far downstream that they im-

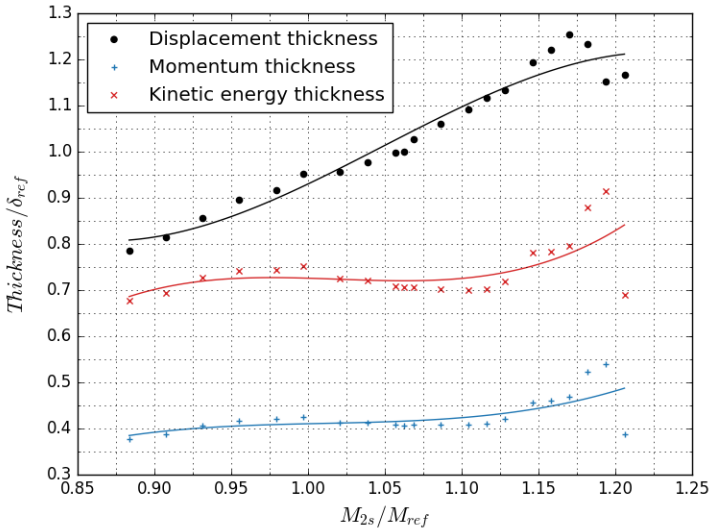


Figure 6.16: Suction surface boundary layer thicknesses of the optimised stator vane with isentropic exit Mach number $M_{2s}$. The reference value $\delta_{ref}$ represents the boundary layer displacement thickness under nominal conditions of $M_{2s}/M_{ref}$ = 1.06. The reference Mach number represents the average target value for the outlet Mach number.

pinge on additional oblique shock waves that are generated near the trailing edge.

As $M_{2s}$ is increased, the oblique shock wave impinging on the suction surface becomes stronger whereas the reflected wave becomes weaker. The former is in agreement with findings of Anand et al. [39], who dictates that the shock strength increases with the degree of divergence in the nozzle. The latter however, is a result of the shock wave impingement location on the curved suction surface. For low $M_{2s}$, the oblique shock impinges on the concave part of the surface upon which several weak reflection waves are generated that point in the same direction. As a result, the weak shocks merge and propagate as a stronger reflection shock wave. For higher $M_{2s}$, the oblique shock impinges on the straight/convex part of the surface. In that case, the reflected waves do not point in the same direction and thus do not merge to former a stronger reflection wave. This effect is visible in Figure C.1, which shows the Schlieren flow visualisations of the baseline stator. As can be seen, the strength of the reflected shock remains rela-

tively constant.

The strength of the oblique shock waves is directly related to the shock loss trend; the shock strength gives an estimate of the stagnation pressure loss as a result of the presence of shocks. However, Mee et al. [1] argue that the influence of the shock angle on the shock loss characteristics is more a consequence of the way the shock loss is determined than a physical feature of the shock structures. The inclination of the shock waves increases with $M_{2s}$ and therefore at higher values of $M_{2s}$ an increasing amount of the loss generated by the shocks will take place further downstream which is then attributed to the loss generated by the trailing edge.

The development of the shock structure is quantitatively assessed by Figure 6.15, which shows the loading of optimised supersonic suction surface for different $M_{2s}$. The presence of oblique shock waves is indicated by a finite drop in the surface isentropic Mach number. For $M_{2s}/M_{ref}$ = 0.88, an oblique shock is observed at $l/l_{max}$ = 0.35. As $M_{2s}/M_{ref}$ is increased to 0.98, the oblique shock moves downstream to $l/l_{max}$ = 0.48 while the shock strength is reduced. Further increasing $M_{2s}/M_{ref}$ to 1.09 moves the oblique shock even more downstream to $l/l_{max}$ = 0.75 while the shock regains its strength. Finally, for $M_{2s}/M_{ref}$ = 1.19, the oblique shock does not impinge on the suction surface anymore but instead interacts with additional trailing edge shocks that are generated at $l/l_{max}$ = 0.8. In this situation, the trailing edge shocks cause the boundary layer to separate, as shown in Figure 6.18D.

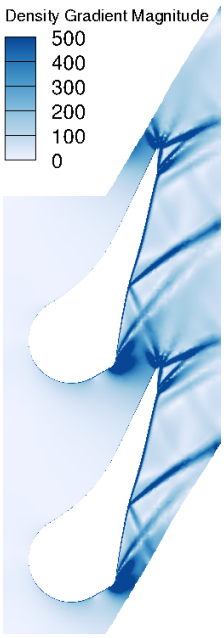


(A) $M_{2s}/M_{ref}$ = 0.88


(B) $M_{2s}/M_{ref}$ = 0.98


(C) $M_{2s}/M_{ref}$ = 1.09


(D) $M_{2s}/M_{ref}$ = 1.19

Figure 6.17: Schlieren flow visualisation of the optimised stator vane for different isentropic exit Mach numbers $M_{2s}$..

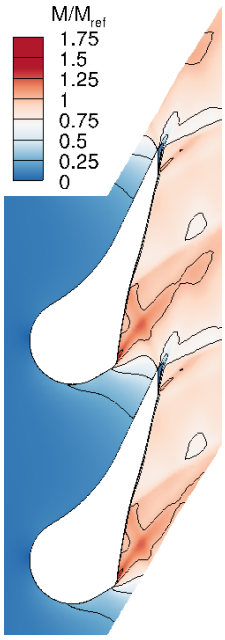


(A) $M_{2s}/M_{ref}$ = 0.88

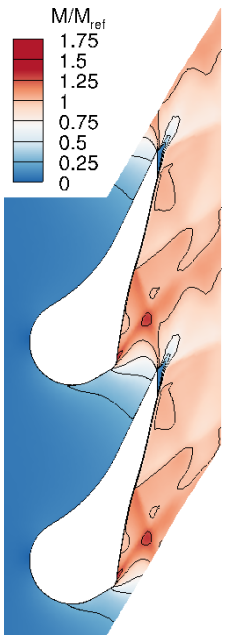


(B) $M_{2s}/M_{ref}$ = 0.98

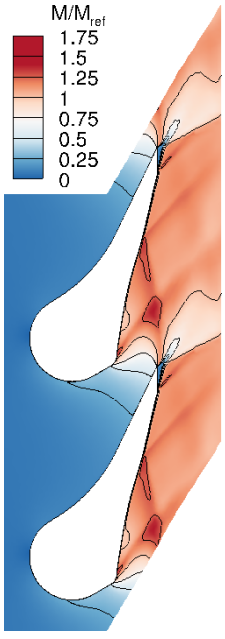


(C) $M_{2s}/M_{ref}$ = 1.09

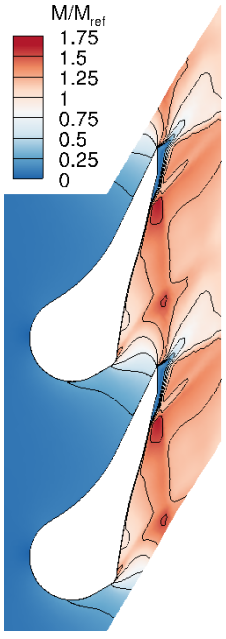


(D) $M_{2s}/M_{ref}$ = 1.19

Figure 6.18: Mach contours of the optimised stator for different isentropic exit Mach numbers $M_{2s}$.. The reference value represents the average target value for the outlet Mach number.

### 6.4.3. Trailing Edge Loss

The variation of the trailing edge loss component is shown in Figure 6.14. The trailing edge component significantly contributes to the total loss and the results suggest that this contribution increases for $M_{2s}/M_{ref} > 1.19$. This increase for even higher $M_{2s}$ numbers can be attributed to the boundary layer separation, which is illustrated in Figure 6.18D. As discussed in subsection 2.2.3, the trailing edge loss is composed of three components: one due to the low base pressure acting on the trailing edge, one for the mixing of the momentum contained in the boundary layers and lastly one representing the simultaneous blockage of the boundary layers and the trailing edge. In the present study, the shape of trailing edge is fixed, so that the trailing edge loss is only dependent upon the base pressure and the components of momentum and displacement thickness. Figure 6.16 and Figure 6.19 show the variation of the boundary layer thickness parameters and the base pressure coefficient with $M_{2s}$, respectively. Recall that the base pressure coefficient is defined by Equation 2.9, where the reference values are now taken at the downstream plane under nominal operating conditions.

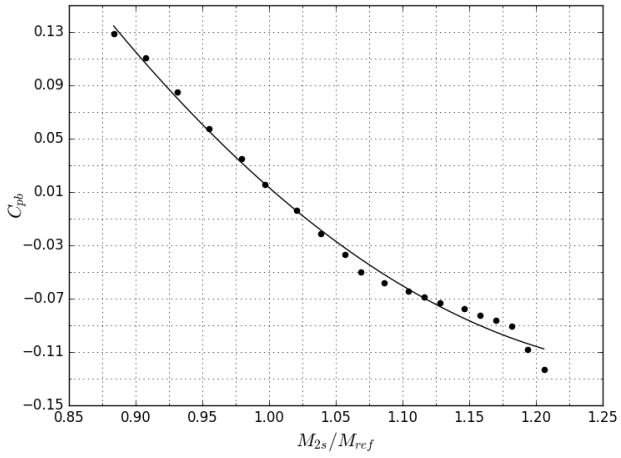


Figure 6.19: Variation of the base pressure coefficient $C_{pb}$ of the optimised stator vane with the isentropic exit Mach number $M_{2s}$. The reference values for the calculation of $C_{pb}$ are taken at the downstream plane under nominal operating conditions. The reference Mach number represents the average target value for the outlet Mach number.

From Figure 6.19 it can be observed that the base pressure coefficient declines with $M_{2s}$. In Figure 6.16 it is also observed that the displacement thickness increases and that the momentum thickness slightly fluctuates with $M_{2s}$. The combined effect however, shown in Figure 6.14, is that the trailing edge loss component varies non-monotonically with $M_{2s}$. The contribution of the base pressure coefficient and the displacement thickness does not seem to compensate for the non-monotonic contribution of the momentum thickness.

### 6.4.4. Total Loss

The trend of the overall loss with $M_{2s}$ is shown in Figure 6.14. The combined effect of the loss components is a relatively constant total loss for 0.88 < $M_{2s}/M_{ref}$ < 1.07. Hereafter, the total loss slightly decreases for 1.07 < $M_{2s}/M_{ref}$ < 1.15. The total loss significantly increases for $M_{2s}/M_{ref}$ > 1.15 and the results suggest that this trend will persist for even higher $M_{2s}$. A remarkable observation is that the total loss of the baseline and optimised stator vane during nominal operation, i.e. $M_{2s}/M_{ref}$ = 1.06, can be reduced by operating at a slightly higher $M_{2s}$, e.g. near $M_{2s}/M_{ref}$ = 1.15.

### 6.4.5. Further Remarks on Off-Design Performance

The turbine inlet manifold supplies the first stage stator vanes of a turbine with hot gases from the combustion chamber. The primary function of the inlet manifold is to evenly distribute the hot gases among the intake ports of the stator vanes. Achieving an even distribution is important to optimise the efficiency of the turbine, but this is hardly possible in reality. Therefore, most of the first stage stator vanes operate in slightly different conditions due to the circumferential non-uniformity induced by manifold. In addition, the turbine experiences different off-design operating conditions during its cycle of operation. The present study is therefore not only concerned with the nominal performance of the optimised stator vane. In Figure 6.14 it can be seen that the optimised stator vane performs better

than the baseline for 0.93 < $M_{2s}/M_{ref}$ < 1.17. The optimised stator vane is therefore expected to perform better for nominal, and a range of off-nominal conditions.

However, there are some operating conditions where the optimised stator vane does not perform better than the baseline, e.g. $M_{2s}/M_{ref}$ = 0.88 and $M_{2s}/M_{ref}$ = 1.19. The change in performance for these conditions can be attributed to the shock loss component, as depicted in Figure 6.14. In Figure 6.20A and Figure 6.17A, which show a numerical Schlieren visualisation of the baseline and optimised design for $M_{2s}/M_{ref}$ = 0.88, respectively, it becomes clear that the oblique shocks impinging on the suction surface are much stronger for the optimised design. This difference is also visible in the Mach contours illustrated in Figure 6.18A and Figure 6.21A. In Figure 6.17D and Figure 6.20B, which show the numerical Schlieren visualisation of the baseline and optimised design for $M_{2s}/M_{ref}$ = 1.19, respectively, it becomes evident that the trailing edge shock system is much more dominant for the optimised design. This is also visible in the Mach contours illustrated in Figure 6.18D and Figure 6.21B.

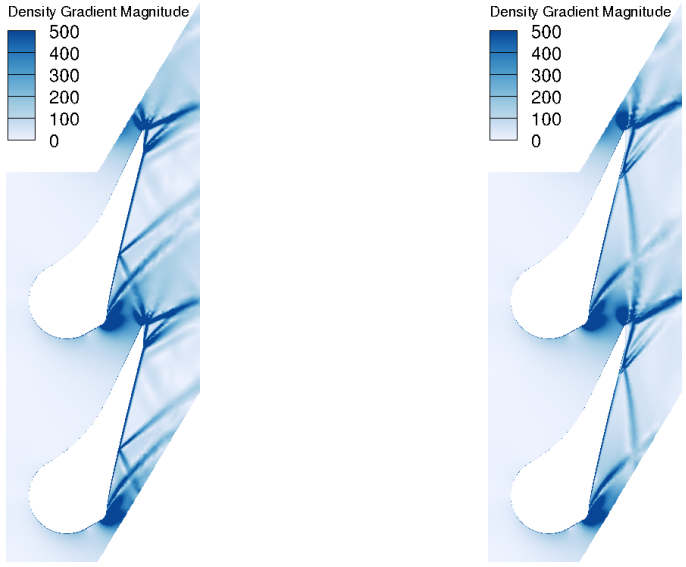


(A) $M_{2s}/M_{ref}$ = 0.88 (B) $M_{2s}/M_{ref}$ = 1.19

Figure 6.20: Numerical Schlieren visualisation of the baseline stator vane by means of the density gradient magnitude for two off-nominal operating conditions.

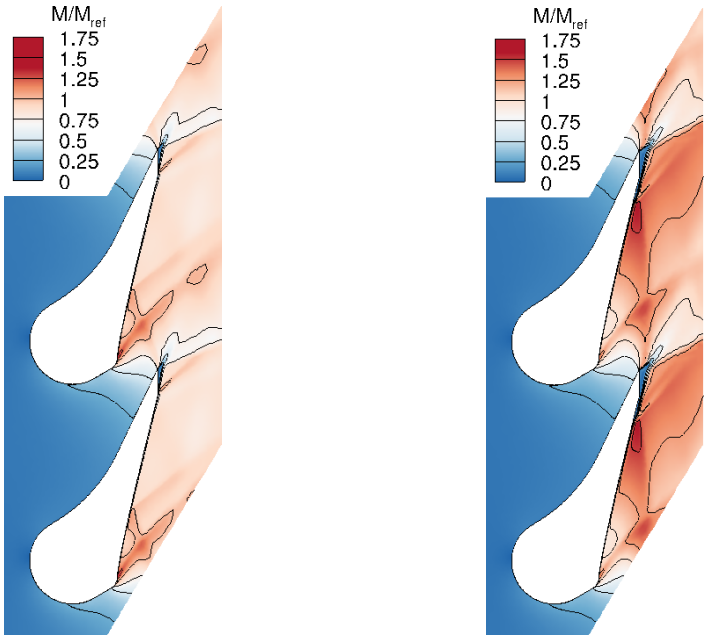


(A) $M_{2s}/M_{ref}$ = 0.88 (B) $M_{2s}/M_{ref}$ = 1.19

Figure 6.21: Mach contours of the baseline stator vane for two off-nominal operating conditions. The reference value represents the average target value for the outlet Mach number.

### 6.4.6. Flow Non-Uniformity

The variation of the area-weighted standard mean deviation of the pitchwise outlet pressure with the isentropic exit Mach number is shown in Figure 6.22. A more uniform pitchwise outlet pressure profile is achieved for the optimised stator vane for $M_{2s}/M_{ref} > 1.00$, and the results suggest that this continues for even higher $M_{2s}$.

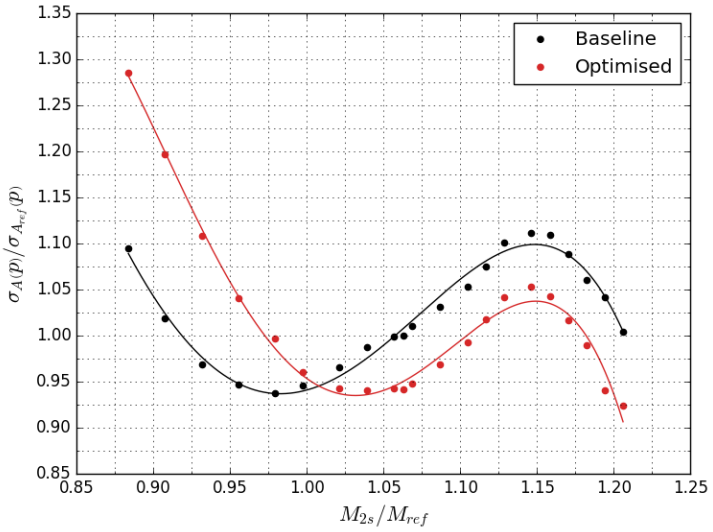


Figure 6.22: Variation of the area-weighted standard mean deviation $\sigma_A$ of the pitchwise outlet pressure with the isentropic exit Mach number $M_{2s}$ for the baseline and optimised stator vane. The reference $\sigma_A\,(p)$ is calculated for the baseline design under nominal operating conditions of $M_{2s}/M_{ref}$ = 1.06. The reference Mach number represents the average target value for the outlet Mach number.

## 6.5. Impact of Stator Performance Improvement on Turbine Performance

The approach adopted in the present study to assess the impact of the stator performance improvement on the overall turbine efficiency is based on the Balje diagram. This approach has been proposed and demonstrated by Souverein et al. [40]. The Balje diagram can be derived from Euler's turbomachinery equation and relates the specific rotational speed $N_s$ and the specific diameter $D_s$ to the turbine efficiency. In this approach, blade loss coefficients are used for the stator and rotor blades to relate the circumferential velocity to the ideal velocity that can be attained for isentropic flow, namely the spouting velocity. The stator and rotor blade loss coefficients are defined as:

$$\psi_N = \frac{u_2}{u_{2s}} \quad \text{and} \quad \psi_R = \frac{w_3}{w_{3s}} \tag{6.2}$$

where $\psi_N$ and $\psi_R$ are the stator and rotor loss coefficients, respectively, $w$ is the relative velocity and the subscript 3 refers to the rotor outlet. Balje [41] shows that the hydraulic turbine efficiency is given by the functional $\eta_h\,(N_s, D_s, r, \alpha_2, \psi_N, \psi_R)$, where $\alpha_2$ is the absolute stator exit angle and $r$ is the degree of reaction. Since the turbine efficiency $\eta$ is smaller than the hydraulic efficiency by the wheel-disk friction loss, an additional term can be included to obtain the functional of $\eta$. The efficiency of an impulse turbine (zero reaction) can now finally be expressed as:

$$\eta = \frac{N_s D_s \sqrt{1 - 2\frac{h}{D} + 2\left(\frac{h}{D}\right)^2}}{77}(1+\psi_R)\left[\psi_N \cos\alpha_2 - \frac{N_s D_s \sqrt{1 - 2\frac{h}{D} + 2\left(\frac{h}{D}\right)^2}}{154}\right] - \frac{N_s^3 D_s^5 16 \beta_w^* \left(1 - 2\frac{h}{D}\right)^5}{154^3} \tag{6.3}$$

where $h$ is the blade height, $D$ is the outer diameter of the rotor and $\beta_W^*$ is the disk-wheel friction coefficient.

Considering now a 2-stage impulse turbine, the overall turbine performance improvement can be evaluated using Equation 6.3. The values of the parameters required for this calculation cannot be disclosed for confidentiality reasons. The results show an increase of about 0.1%. The impact on the overall performance is not staggering, but considering that the optimisation was quite constrained, this does not come as a surprise.

In addition, the calculation of the turbine efficiency involves the assumption of a constant rotor loss coefficient. The decreased flow non-uniformity at the stator outlet might have a beneficial impact on the rotor loss coefficient and thus on the overall turbine performance. However, these interpretations are speculative, and any conclusions concerning the effectiveness of the stator optimisation on the overall turbine performance must be based on the results of an impact study.

# Chapter 7

# Conclusions and Recommendations

This is a concluding chapter explaining the scientific and technical implications of the research findings in considerable detail. Recommendations for further works will also be provided.

## 7.1. Conclusions

During the preliminary design of turbines the two-dimensional losses must be modelled before a detailed design can be performed on the blade shape. To define an initial design configuration, turbomachinery engineers rely on mean-line and throughflow models that are based on empirical loss correlations, but these are often derived from cascade experiments and numerical analyses that do not apply to supersonic blades. Axial turbines for rocket propulsion applications are characterised by supersonic stator vanes that yield a complex flow field, making the prediction of losses challenging with existing correlations. The research questions were therefore formulated as:

- *What is the impact of the isentropic exit Mach number on the profile losses in supersonic axial turbine stator vanes for rocket propulsion applications?*
- *What reduction of the profile losses in supersonic axial turbine stator vanes for rocket propulsion applications can be achieved using the adjoint optimisation method?*

The current study presented an investigation of the physical origins of the two-dimensional loss mechanisms in supersonic axial turbine stator vanes. The investigation has been realised through the study of a stator vane that is applied in the first turbine stage of a 1MN-class gas generator type rocket engine. The performance of the stator vane is first improved by exploiting a fluid dynamic design optimisation framework that leverages on a RANS adjoint solver incorporated in the open-source SU2 suite. The optimisation is focused on the supersonic suction surface because performance, manufacturing and thermomechanical constraints have made it challenging to optimise the entire stator vane.
The main contributions of the present study can be summarised as follows:

- A loss breakdown method based on the kinetic energy dissipation is conceived and developed by using the energy loss coefficient in different forms. The loss breakdown method is validated using the transonic LS89 turbine blade and showed strong agreement with experimental data.
- The adjoint optimisation of the supersonic suction surface led to a 6% reduction in the entropy generation coefficient and a 0.1% increase in the overall turbine efficiency of an assumed 2-stage impulse turbine. The optimised surface has a concave shape in the throat region and a convex shape towards the trailing edge. The combined effect is a less pronounced flow acceleration and consequently weaker shocks, whereas the boundary layer and trailing edge loss have remained nearly constant. In addition, the standard mean deviation of the pitchwise outlet pressure is reduced by 6%; this is a direct consequence of adopting the mixed-out averaging procedure for calculating the entropy generation coefficient. The expected benefit is a weakening of the stator-rotor interaction.
- The variation of the two-dimensional loss components with the isentropic exit Mach number $M_{2s}$ has been investigated. In general, the boundary layer loss decreases monotonically with $M_{2s}$ and the results

suggest that this trend continues for even higher $M_{2s}$. The shock and trailing edge loss components show non-monotonic behaviour. The shock loss peaks near nominal operating conditions, the inverse holds for the trailing edge loss. Numerical Schlieren visualisations have revealed that this is caused by the complex shock patterns that are observed in the flow passage. As $M_{2s}$ is increased, the oblique shocks impinging on the supersonic suction surface move downstream while the shock angles are reduced. The oblique shock impinging on the surface increases in strength, whereas its reflection decreases in strength. A further increase in $M_{2s}$ even results in shock wave-wake interaction. The results suggest that the shock and trailing edge loss increase for even higher $M_{2s}$. The overall loss is relatively constant and only significantly increases for $M_{2s}$ where effects of shock-wake interaction become prominent.

In summary, there are two relevant outcomes of the present study:

- The shock loss is the primary loss component in supersonic axial turbine stator vanes. The magnitude of the shock loss component depends on the shock impingement location on the supersonic suction surface.
- In order to improve the performance of supersonic axial turbine stator vanes, the supersonic suction surface must be carefully designed in order to control the shock structures.

## 7.2. Recommendations

The present study has led to a better understanding of the two-dimensional loss mechanisms in supersonic turbine stator vanes and the adjoint method has been implemented to improve the stator performance. The quality of the present study may be improved in several ways, of whom the most important are suggested below.

- Flow physics of the complex shock patterns and their interaction with the boundary layer and trailing edge wake may be better captured using higher-order methods. In this regards, a more accurate approach to turbulence modelling, e.g. Reynolds Stress Models or LES, could further increase the quality of the results achieved in this study. This could lead to a more accurate prediction of the loss components.
- The unconventional optimisation convergence may imply that the SLSQP algorithm is burdened by the intricate nature of supersonic flow. Perhaps its a consequence of confining the FFD box to the supersonic suction surface. The computational framework could be extended to include more robust optimisation algorithms for constrained non-linear problems. In this way the endless endeavours of defining a stable optimisation could be avoided. This could lead to a computational advantage and a better performance improvement.
- A less constrained optimisation could lead to a more significant performance improvement. It is expected that the sharp and straight trailing edge shape have a substantial impact on the performance. In particular, for the additive manufacturing method, further optimisations should be performed for a fixed throat section, angle upstream of the throat and trailing thickness, but permitting more variation in the blade profile, notably the trailing edge profile. This might result in designs that require the framework to be adapted to handle large mesh deformations.
- A particularly interesting type of multi-objective shape design is represented by a multi-point optimisation. In this approach, the cost function is calculated at different operating conditions during each optimisation step. This type of optimisation allows to address flow problems that are intrinsically linked to relevant fluctuations of the operating conditions. This design methodology may lead to more robust stator vanes whose performance is less sensitive to variations of the operating conditions.

# Appendix A

# Loss Breakdown Methodology for Subsonic & Transonic Blades

This appendix provides an overview of the two-dimensional loss breakdown method for subsonic and transonic blades.

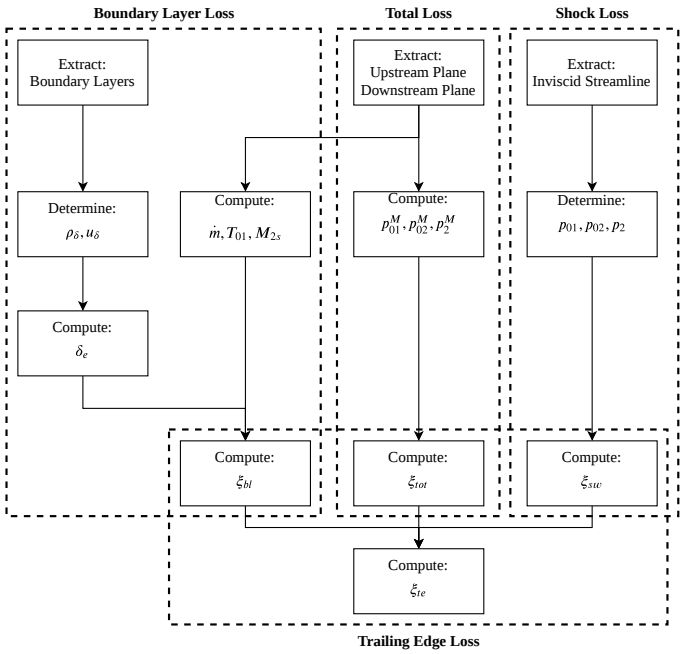


Figure A.1: Overview of the two-dimensional loss breakdown method for subsonic and transonic blades, where the superscript $M$ indicates a mass-weighted average. The loss components and the total loss are expressed in terms of the energy loss coefficient $\xi$ and it is assumed that the working fluid is fixed and behaves like a calorically perfect gas. Stations 1 and 2 refer to the upstream and downstream plane, respectively.

# Appendix B

# Loss Trends with Reynolds Number

This appendix provides the variation of the loss components with the axial chord Reynolds number.

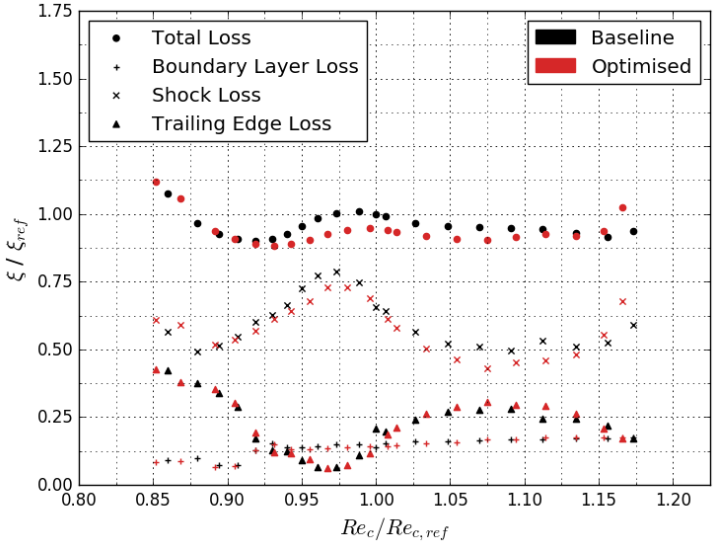


Figure B.1: Variation of the loss components in terms of the energy loss coefficient $\xi$ with the axial chord Reynolds number $Re_c$. The reference loss coefficient represents the total loss coefficient of the baseline design under nominal operating conditions of $Re_{c,ref}$.

# Appendix C

# Numerical Schlieren Visualisation of Baseline Design

This appendix provides numerical Schlieren visualisations of the baseline stator vane.


(A) $M_{2s}/M_{ref}$ = 0.88


(B) $M_{2s}/M_{ref}$ = 0.98


(C) $M_{2s}/M_{ref}$ = 1.09


(D) $M_{2s}/M_{ref}$ = 1.19

Figure C.1: Numerical Schlieren flow visualisation of the baseline stator vane for different isentropic exit Mach numbers $M_{2s}$.

# References


[1] D. J. Mee, N. C. Baines, M. L. G. Oldfield, and T. E. Dickens, "An examination of the contributions to loss on a transonic turbine blade in cascade", *Journal of Turbomachinery*, vol. 114, no. 1, pp. 155–162, Jan. 1, 1992.

[2] H. W. Douglas, "Liquid rocket engine turbines", National Aeronautics and Space Administration (NASA), Cleveland, Ohio, United States, Technical Report NASA-SP-8110, Jan. 1, 1974.

[3] J. D. Denton, "The 1993 IGTI scholar lecture: Loss mechanisms in turbomachines", *Journal of Turbomachinery*, vol. 115, no. 4, pp. 621–656, Oct. 1, 1993.

[4] G. Paniagua and J. Steelant, Eds., *Advances on propulsion technology for high-speed aircraft. volume 1*, Mar. 2007.

[5] D. J. Dorney, L. W. Griffin, F. Huber, and D. L. Sondak, "Unsteady flow in a supersonic turbine with variable specific heats", *Journal of Propulsion and Power*, vol. 18, no. 2, pp. 493–496, 2002.

[6] A. J. Glassman, *Turbine design and application volumes 1, 2, and 3*, Jun. 1, 1994.

[7] E. M. Greitzer, C. S. Tan, and M. B. Graf, *Internal Flow: Concepts and Applications*. Cambridge: Cambridge University Press, 2004.

[8] W. N. Dawes, "A comparison of zero and one equation turbulence modelling for turbomachinery calculations", presented at the ASME 1990 International Gas Turbine and Aeroengine Congress and Exposition, American Society of Mechanical Engineers Digital Collection, 1990.

[9] A. D. Young, *Boundary Layers*. American Institute of Aeronautics and Astronautics, 1989, 296 pp.

[10] F. M. White, *Viscous Fluid Flow*. McGraw-Hill, 1991.

[11] Hermann Schlichting, *Boundary Layer Theory*, Sixth Edition. New York: McGraw-Hill, 1968.

[12] E. Truckenbrodt, "A method of quadrature for calculation of the laminar and turbulent boundary layer in case of plane and rotationally symmetrical flow", National Advisory Committee for Aeronautics, May 1, 1955.

[13] A. H. Shapiro, *The dynamics and thermodynamics of compressible fluid flow*. New York: John Wiley & Sons, 1953, vol. One.

[14] J. D. J. Anderson, *Fundamentals of Aerodynamics*, Fifth edition. McGraw-Hill, 2011, 1106 pp.

[15] C. Hall and S. L. Dixon, *Fluid Mechanics and Thermodynamics of Turbomachinery*, Seventh. Butterworth-Heinemann, Oct. 10, 2013, 556 pp.

[16] C. J. Atkin and L. C. Squire, "A study of the interaction of a normal shock wave with a turbulent boundary layer at mach numbers between 1.30 and 1.55", *European Journal of B/Fluids*, vol. 11, no. 1, pp. 93–118, 1992.

[17] L. J. Souverein, P. G. Bakker, and P. Dupont, "A scaling analysis for turbulent shock-wave/boundary-layer interactions", *Journal of Fluid Mechanics*, vol. 714, pp. 505–535, Jan. 2013.

[18] J. B. Young and R. C. Wilcock, "Modeling the air-cooled gas turbine: Part 2—coolant flows and losses", *Journal of Turbomachinery*, vol. 124, no. 2, pp. 214–221, Apr. 9, 2002.

[19] H. Tennekes and J. L. Lumley, *A First Course in Turbulence*. MIT Press, 1972, 320 pp.

[20] J. H. Ferziger and M. Perić, *Computational methods for fluid dynamics*, 3rd, rev. ed. Berlin ; New York: Springer, 2002, 423 pp.

[21] F. R. Menter, "Two-equation eddy-viscosity turbulence models for engineering applications", *AIAA Journal*, vol. 32, no. 8, pp. 1598–1605, Aug. 1994.

[22] M. B. Giles and N. A. Pierce, "An introduction to the adjoint approach to design", *Flow, Turbulence and Combustion*, vol. 65, no. 3, pp. 393–415, Dec. 1, 2000.

[23] M. Pini, "Turbomachinery design optimization using adjoint method and accurate equations of state", PhD thesis, Politecnico di Milano, Milan, Dec. 2013.

[24] M. Pini, G. Persico, D. Pasquale, and S. Rebay, "Adjoint method for shape optimization in real-gas flow applications", *Journal of Engineering for Gas Turbines and Power*, vol. 137, no. 3, p. 032 604, Mar. 1, 2015.

[25] S. Vitale, T. A. Albring, M. Pini, N. R. Gauger, and P. Colonna, "Fully turbulent discrete adjoint solver for non-ideal compressible flow applications", *Journal of the Global Power and Propulsion Society*, vol. 1, Z1FVOI, Nov. 22, 2017.

[26] J. A. Samareh, "Survey of shape parameterization techniques for high-fidelity multidisciplinary shape optimization", *AIAA Journal*, vol. 39, no. 5, pp. 877–884, May 2001.

[27] J. Samareh, "Aerodynamic shape optimization based on free-form deformation", in *10th AIAA/ISSMO Multidisciplinary Analysis and Optimization Conference*, Albany, New York: American Institute of Aeronautics and Astronautics, Aug. 30, 2004.

[28] N. Anand, S. Vitale, P. Colonna, and M. Pini, "Assessment of FFD and CAD-based shape parametrization methods for adjoint-based turbomachinery shape optimization.", p. 9, May 2018.

[29] R. P. Dwight, "Robust mesh deformation using the linear elasticity equations", in *Computational Fluid Dynamics 2006*, H. Deconinck and E. Dick, Eds., Berlin, Heidelberg: Springer, 2006, pp. 401–406.

[30] S. Vitale, "Advancements in automated design methods for NICFD turbomachinery", PhD thesis, Delft University of Technology, Delft, 2018.

[31] T. D. Economon, F. Palacios, S. R. Copeland, T. W. Lukaczyk, and J. J. Alonso, "SU2: An open-source suite for multiphysics simulation and design", *AIAA Journal*, vol. 54, no. 3, pp. 828–846, Mar. 2016.

[32] M. B. Giles, "Nonreflecting boundary conditions for euler equation calculations", *AIAA Journal*, vol. 28, no. 12, pp. 2050–2058, Dec. 1990.

[33] L. E. Brown, "Axial flow compressor and turbine loss coefficients: A comparison of several parameters", *Journal of Engineering for Power*, vol. 94, no. 3, pp. 193–201, Jul. 1, 1972.

[34] D. J. Mee, N. C. Baines, and M. L. G. Oldfield, "Detailed boundary layer measurements on a transonic turbine cascade", *Journal of Turbomachinery*, vol. 114, no. 1, pp. 163–172, Jan. 1, 1992.

[35] M. Oldfield, D. Schultz, and J. Nicholson, "Loss measurements using a fast traverse in an ILPT transient cascade", presented at the Symposium on Measuring Techniques for Transonic and Supersonic Flows in Cascades and Turbomachines, Lyon, 1981, MTT0681–A517.

[36] T. Arts, M. Lambert de Rouvroit, and A. Rutherford, "Aero-thermal investigation of a highly loaded transonic linear turbine guide vane cascade", Von Karman Institute for Fluid Dynamics, 1990, p. 97.

[37] P. Duan, C. S. Tan, A. Scribner, and A. Malandra, "Loss generation in transonic turbine blading", *Journal of Turbomachinery*, vol. 140, no. 4, p. 041 006, Feb. 6, 2018.

[38] F. Palacios, T. D. Economon, and J. J. Alonso, "Large-scale aircraft design using SU2", in *53rd AIAA Aerospace Sciences Meeting*, Kissimmee, Florida: American Institute of Aeronautics and Astronautics, Jan. 5, 2015.

[39] N. Anand, S. Vitale, M. Pini, G. J. Otero, and R. Pecnik, "Design methodology for supersonic radial vanes operating in nonideal flow conditions", *Journal of Engineering for Gas Turbines and Power*, vol. 141, no. 2, p. 022 601, Feb. 1, 2019.

[40] L. Souverein, L. Veggi, S. Sudhof, R. Behr, and O. Haidn, "On the effect of axial turbine rotor blade design on efficiency: A parametric

study of the baljé-diagram", presented at the 7th European Conference for Aeronautics and Space Sciences (EUCASS), Politecnico di Milano: EUCASS, Jul. 2017.

[41] O. E. Balje´, "A study on design criteria and matching of turbomachines: Part a—similarity relations and design criteria of turbines", *Journal of Engineering for Power*, vol. 84, no. 1, pp. 83–102, Jan. 1, 1962.